FULL PAPER

Onboard software of Plasma Wave Experiment aboard Arase: instrument management and signal processing of Waveform Capture/Onboard Frequency Analyzer

Shoya Matsuda[1*] , Yoshiya Kasahara[2], Hirotsugu Kojima[3], Yasumasa Kasaba[4], Satoshi Yagitani[2], Mitsunori Ozaki[2], Tomohiko Imachi[2], Keigo Ishisaka[5], Atsushi Kumamoto[4], Fuminori Tsuchiya[4], Mamoru Ota[2], Satoshi Kurita[1], Yoshizumi Miyoshi[1], Mitsuru Hikishima[6], Ayako Matsuoka[6] and Iku Shinohara[6]

Abstract

We developed the onboard processing software for the Plasma Wave Experiment (PWE) onboard the Exploration of energization and Radiation in Geospace, Arase satellite. The PWE instrument has three receivers: Electric Field Detector, Waveform Capture/Onboard Frequency Analyzer (WFC/OFA), and the High-Frequency Analyzer. We designed a pseudo-parallel processing scheme with a time-sharing system and achieved simultaneous signal processing for each receiver. Since electric and magnetic field signals are processed by the different CPUs, we developed a synchronized observation system by using shared packets on the mission network. The OFA continuously measures the power spectra, spectral matrices, and complex spectra. The OFA obtains not only the entire ELF/VLF plasma waves' activity but also the detailed properties (e.g., propagation direction and polarization) of the observed plasma waves. We performed simultaneous observation of electric and magnetic field data and successfully obtained clear wave properties of whistler-mode chorus waves using these data. In order to measure raw waveforms, we developed two modes for the WFC, 'chorus burst mode' (65,536 samples/s) and 'EMIC burst mode' (1024 samples/s), for the purpose of the measurement of the whistler-mode chorus waves (typically in a frequency range from several hundred Hz to several kHz) and the EMIC waves (typically in a frequency range from a few Hz to several hundred Hz), respectively. We successfully obtained the waveforms of electric and magnetic fields of whistler-mode chorus waves and ion cyclotron mode waves along the Arase's orbit. We also designed the software-type wave–particle interaction analyzer mode. In this mode, we measure electric and magnetic field waveforms continuously and transfer them to the mission data recorder onboard the Arase satellite. We also installed an onboard signal calibration function (onboard SoftWare CALibration; SWCAL). We performed onboard electric circuit diagnostics and antenna impedance measurement of the wire-probe antennas along the orbit. We utilize the results obtained using the SWCAL function when we calibrate the spectra and waveforms obtained by the PWE.

Keywords: Arase satellite, ERG, PWE, Plasma wave, Geospace, Radiation belt, Onboard processing, Chorus wave, EMIC wave, Magnetosonic wave

---

*Correspondence: matsuda@isee.nagoya-u.ac.jp
[1] Institute for Space-Earth Environmental Laboratory, Nagoya University, Chikusa-ku, Nagoya 464-8601, Japan
Full list of author information is available at the end of the article

Matsuda *et al. Earth, Planets and Space* (2018) 70:75

Page 2 of 22

Introduction

Recent observations and simulation studies suggest that the whistler-mode chorus wave has an important role in the internal acceleration of radiation belt electrons (Foster et al. 2017; Katoh and Omura 2007; Reeves et al. 2013; Li et al. 2014). The significant loss of relativistic electron and energetic ion precipitation due to electromagnetic ion cyclotron (EMIC) waves is a remarkable wave–particle interaction process in the inner magnetosphere (Albert 2003; Cornwall 1965; Horne and Thorne 1998; Jordanova et al. 2007; Lyons et al. 1972; Meredith et al. 2003; Thorne and Kennel 1971). The inner magnetosphere is typically defined as the region where L values < 7, that includes the plasmasphere, the ring current, and the Van Allen radiation belts. The Exploration of energization and Radiation in Geospace, Arase (ERG) satellite was launched on December 20, 2016, to understand dynamics around the Van Allen radiation belt such as particle acceleration, loss mechanisms, and the dynamic evolution of space storms in the context of cross-energy and cross-regional coupling (Miyoshi et al. 2012). The Plasma Wave Experiment (PWE) is one of the scientific instruments onboard the Arase satellite and is used to measure the electric field and magnetic field in the inner magnetosphere (Kasahara et al. 2018). We will focus on the measurement of the electric field evolution and the natural plasma wave related to the inner magnetospheric dynamics. High-qualification measurements of such plasma waves by the PWE contribute to our understanding of the inner magnetospheric dynamics. The Arase satellite challenges direct measurements of the wave–particle interaction (energy transfer between plasma particles and waves) using the coordinated observation of plasma particle detectors (Medium-Energy Particle Experiments—Electron Analyzer; MEP-e, High-Energy Electron Experiments; HEP, and Extremely High-Energy Electron Experiment; XEP) and the PWE. One of the important tasks of the PWE is the synchronized measurements of the waveforms of electric and magnetic fields and the transfer of the observed waveforms to the software-type wave–particle interaction analyzer (S-WPIA) (Hikishima et al. 2018; Katoh et al. 2018) onboard the Arase satellite. Our project focuses not only on simple in situ measurements but also on satellite-ground conjugate observations. In situ high time resolution measurements in the inner magnetosphere and simultaneous ground optical measurements (e.g., Ozaki et al. 2015), VLF wave measurements (e.g., Martinez-Calderon et al. 2016), and radar observations (e.g., Miyoshi et al. 2015) can be used to clarify one-to-one correspondence of space and ground phenomena. In situ measurements by Arase and ground-based measurements by the PWING (study of dynamical variation of Particles and Waves in the INner magnetosphere using Ground-based network observations) project can also contribute to understand the mechanism of plasma particle precipitation by wave–particle interaction (Shiokawa et al. 2017). In order to achieve these objectives, we developed an advanced onboard processing technique and implemented it into the PWE. In the present paper, we will describe the detailed specifications of the onboard processing of the PWE and introduce its initial observation results.

Requirements for the onboard software

Figure 1 shows an overview of the PWE (Kasahara et al. 2018). The PWE consists of two sensors, two CPU boards, and three receivers. The two CPUs are connected using the SpaceWire protocol. They receive telemetry commands from the satellite bus-system and should appropriately recognize and change their behaviors (e.g., observation modes). The housekeeping (HK) data production is important for the notification of the instrument's status. Two CPU boards (CPU #8 and CPU #9) mainly process electric field data and magnetic field data, respectively. Telemetry command communication and HK sharing between the two CPUs are required for the coordinated observation of electric and magnetic fields.

The PWE covers frequency range from DC to 10 MHz for electric field, and from a few Hz to 100 kHz for magnetic field by the following receivers: Electric Field Detector (EFD) (Kasaba et al. 2017) for the measurement of electric field from DC to 256 Hz, Waveform Capture/ Onboard Frequency Analyzer (WFC/OFA) for the measurement of electric field and magnetic field from a few Hz to 20 kHz, and the High-Frequency Analyzer (HFA) (Kumamoto et al. 2018) for the measurement of electric field from 10 kHz to 10 MHz and magnetic field from 10 to 100 kHz. Each receiver focuses on the measurements of the following issues (for more details, see Kasahara et al. 2018):

- EFD (Kasaba et al. 2017)

  - Continuous measurement of the DC electric field.
  - Continuous observation of low-frequency electric field waveform (for the measurement of EMIC waves).

Matsuda *et al. Earth, Planets and Space* (2018) 70:75

Page 3 of 22

- Raw (512 samples/s) electric field waveform observation by a telemetry command and the auto-triggering.

- OFA

  - Continuous measurement of electric and magnetic field auto-spectra. We need them as a survey data for the selective downlink of observed waveforms.
  - Simultaneous and continuous observation of electric and magnetic field cross-spectra. This is for the direction finding and polarization analyses of observed plasma waves.

- WFC

  - Command triggered or auto-triggered waveform observation of electric and magnetic fields for the analyses of whistler-mode plasma waves [e.g., rapid frequency sweeping of a chorus wave element (Summers et al. 2012; Li et al. 2011)] and that for the analyses of ion cyclotron mode waves [e.g., multi-band structure of EMIC waves (Meredith et al. 2014; Sakaguchi et al. 2013) and/or nonlinear EMIC triggered emissions (Grison et al. 2016; Nakamura et al. 2015; Pickett et al. 2010)].
  - Raw electric and magnetic field waveform production for the S-WPIA mode operation.

- HFA (Kumamoto et al. 2018)

  - Continuous measurement of the upper hybrid resonance (UHR) wave for the determination of electron number density.
  - High-resolution spectrum measurement of high-frequency plasma waves [e.g., auroral kilometric radiation (AKR) and continuum radiation].
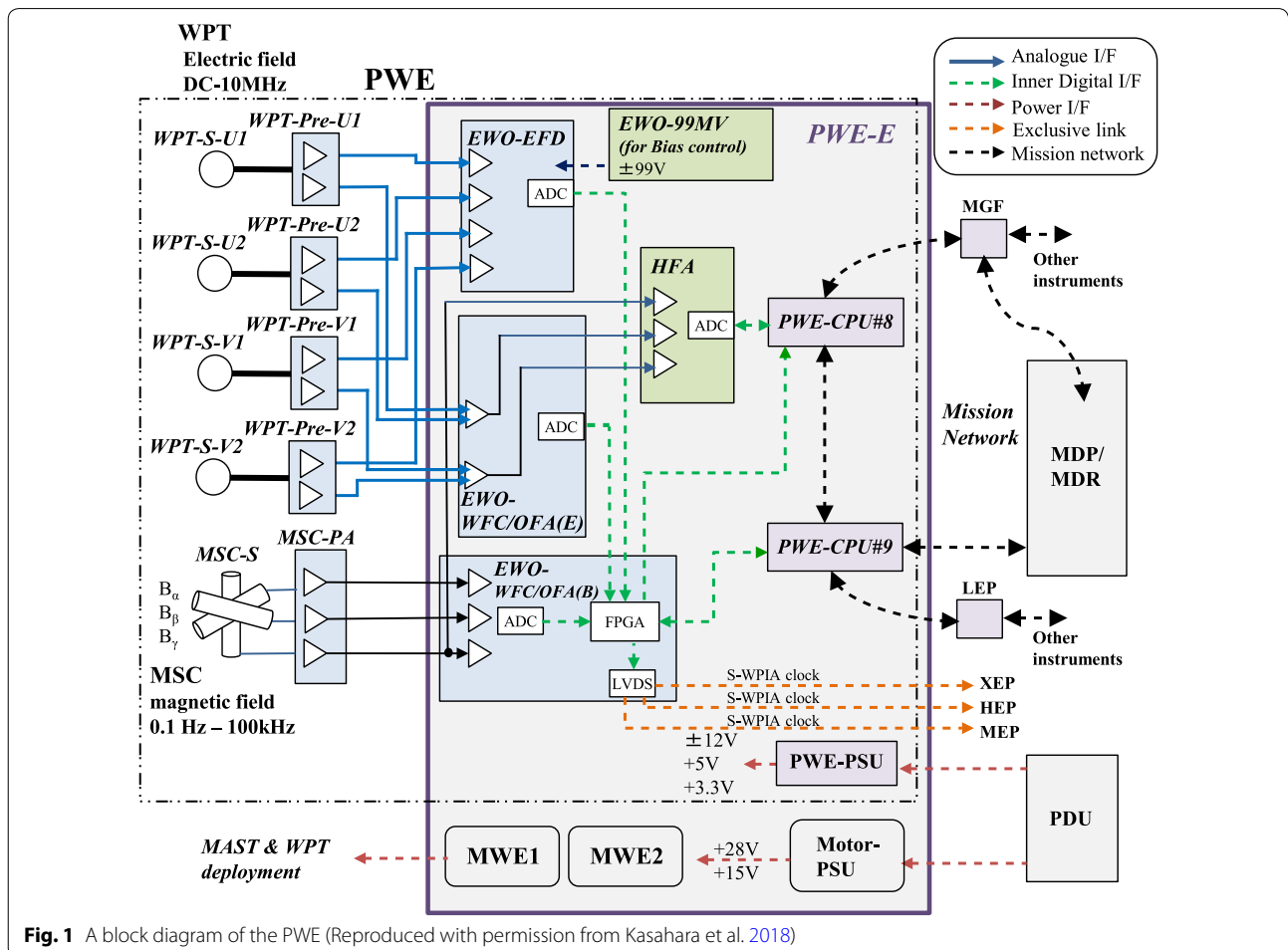
Fig. 1 A block diagram of the PWE (Reproduced with permission from Kasahara et al. 2018)

Matsuda *et al. Earth, Planets and Space* (2018) 70:75

Page 4 of 22

The mission data produced by the PWE instrument is roughly divided into two types: 'continuous data' and 'burst data.' All products produced by the EFD, OFA, and HFA are categorized as continuous data [except for the raw (512 samples/s) electric field waveform observed by the EFD]. They are always generated when the PWE status is ON. As a general rule, all of the observed continuous data are transferred to the ground. They are used for a survey view of the entire observation. On the other hand, raw waveforms observed by the EFD and WFC are categorized as burst data. They are generated intermittently by a telemetry command or from onboard triggering (e.g., raw waveforms for the high-resolution analyses). Since the data quantity of the burst data is large, the observed burst data are accumulated once in the mission data recorder (MDR). We then need to decide on the priority of the observed burst data and transfer the selected data to the ground. In order to achieve such a selective downlink, we first obtain and survey continuous data. After surveying, we select burst data candidates and transfer them to the ground.

The common important task of each receiver is performing continuous measurement of the 'continuous data.' Additionally, 'burst data' production is also important tasks for the EFD and the WFC. For the OFA, simultaneous observation of electric and magnetic field cross-spectra is important to determine phase differences between electric and magnetic fields.

The S-WPIA measures $E \cdot v$ with 10 μs time accuracy, where E and v denote electric field vector of a plasma wave and a particle velocity vector, respectively (Hikishima et al. 2018; Katoh et al. 2018). In order to achieve S-WPIA measurements, time accuracy of the observed waveform by PWE needs to be < 10 μs.

Overview and architecture of the onboard software
Application layers
The onboard software of the PWE was constructed on middleware and real-time OS kernels. The software has seven application layers, and they operate in pseudo-parallel using a time-sharing process. Table 1 shows an overview of each task assigned to each application layer. Each application is activated by App01 every specified period ('activation frequency' shown in Table 1). Priorities are defined for all applications as shown in Table 1. The high-priority tasks are preferentially performed, and low-priority tasks are performed in spare time.

App01 App01 controls the multitasking system. It activates App02–App07 with its activation.

App02 App02 performs command processing. It receives commands for the PWE and sends commands to the EWO (EFD, WFC, and OFA)/HFA receivers.

App03 App03 performs housekeeping (HK) data processing. It analyzes HK data from the EWO/HFA receivers and generates HK telemetry to send to the ground.

App04 App04 processes observed signals received by the EWO/HFA receivers and generates the continuous data.

App05 App05 performs data processing for special functions (e.g., onboard calibration function).

App06 App06 generates S-WPIA mode waveforms and sends them to the MDR.

App07 App07 processes observed signals received by the EWO receiver and generates the burst data.

Signal buffers
Raw waveforms (and some processed data) generated by the EWO receiver and the HFA receivers are stored to the ring buffer (long buffer and short buffer) on the CPU board. For the EWO receiver, sampling rates of EFD waveform and that of WFC waveform are 512 Hz and 65.536 kHz, respectively. The size of long and short buffers and the bit rates of data obtained by the each receiver are shown in Table 2.
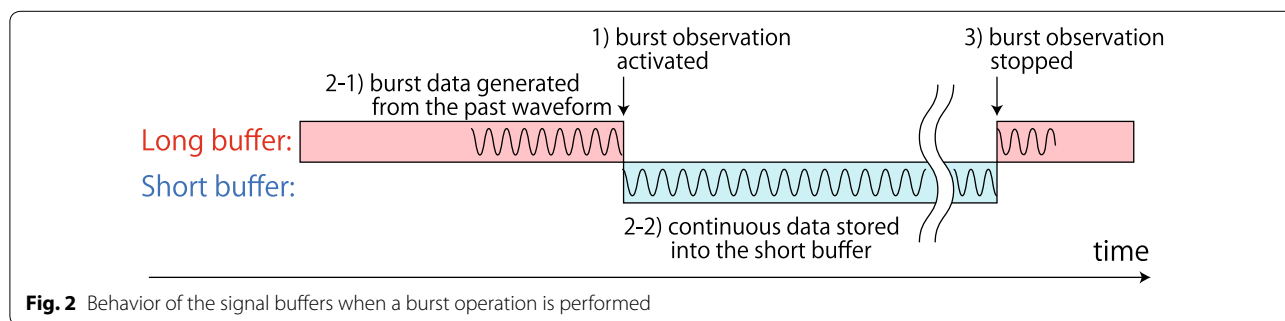
Figure 2 shows the behavior of the two buffers. The observation data are always processed from the long buffer in the nominal operation mode. When we need to hold

Table 1 Priority, activation frequency, and assigned tasks of each application layer

Priority	Activation frequency (Hz)	App number	Tasks
1	16	App01	Time scheduling of each application
2	1	App02	Command processing
3	1	App03	HK data generation
4	1/4	App06	S-WPIA data generation
5	1/4	App04	Continuous data processing (EFD, OFA, and HFA)
6	1/4	App05	Special function data processing (SWCAL)
7	1/4	App07	Burst data processing (EFD and WFC)

Matsuda *et al. Earth, Planets and Space* (2018) 70:75

Page 5 of 22

Table 2 Configuration of the long buffer and the short buffer on the CPUs

Receiver	Data rate (MB/s)	Buffer size (MB) (short buffer)	Buffer size (MB) (long buffer)	Maximum recording time (s) (short buffer)	Maximum recording time (s) (long buffer)
CPU #8					
EWO	0.271	4.5	84	16.6	310
HFA	0.041	3.4	3.4	83	83
CPU #9					
EWO	0.397	5.2	87	13.1	219

Fig. 2 Behavior of the signal buffers when a burst operation is performed

data for a long time (during waveform compression or data processing by the CPU), the data stored in the long buffer are frozen and the latest data are stored into the short buffer. After the processing is completed, the destination of the observation data is switched again to the long buffer.
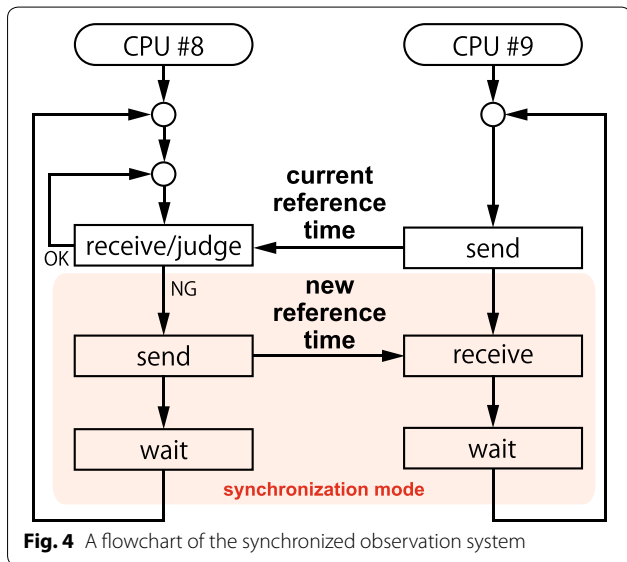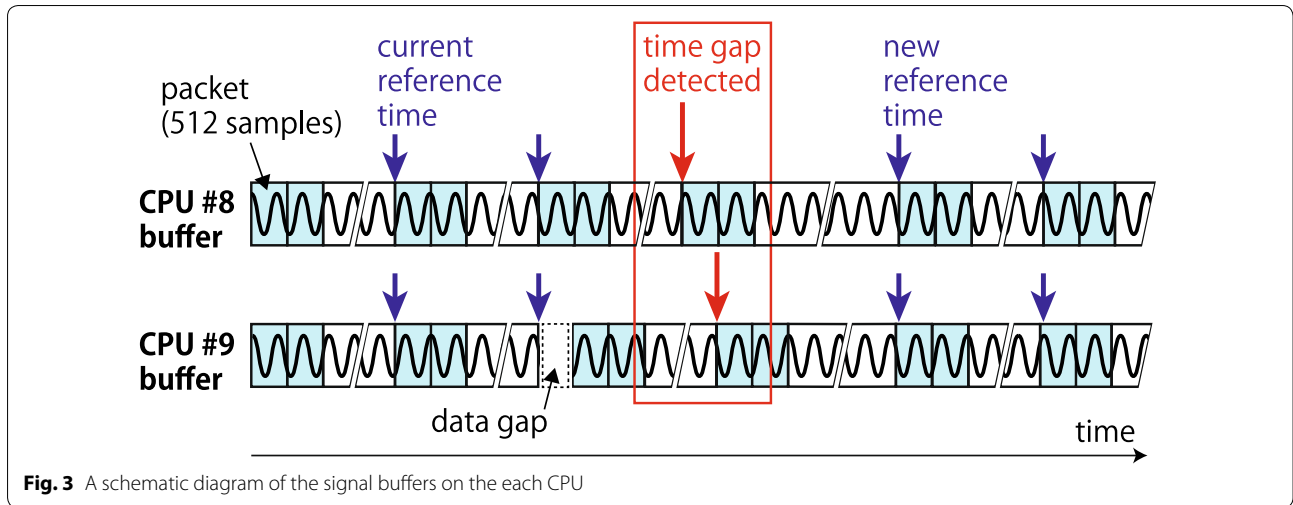
Time determination

The EWO and HFA receivers receive Time Index (TI) from satellite bus-system at every spin (approximately 8 s period). The least significant bit (LSB) of the TI corresponds to 1/64 s. A TI generated by the bus-system can be converted into a corresponding UTC by the time calibration system on the ground. The EWO receiver has a unique time counter (named 'S-WPIA counter'). The S-WPIA counter is reset when the EWO receiver receives new TI from the satellite bus-system. The LSB of the S-WPIA counter corresponds to 1/524,288 s. In order to achieve the requirement of the time accuracy for the S-WPIA measurement, we attached a set of instantaneous TI and S-WPIA counter on to the data observed by the EWO and HFA receivers.

Synchronized observation

For the reason of the limited resources on the onboard CPUs, electric and magnetic field spectra are generated from intermittent waveforms by the OFA (shown in the next section). In order to obtain instantaneous phase differences between electric and magnetic fields, a time window of electric field waveform needs to coincide with that of magnetic field. Since the electric and magnetic

field packets are collected and processed by the different CPUs, we need a time-synchronization system for the simultaneous observation. Figure 3 shows a schematic diagram of the signal buffers on the each CPU. The CPU stores each 512 samples waveform into a data packet (small rectangles). For example, we collect 1024 samples (2 packets, shown as blue box) every 65,536 samples (128 packets) when we perform 1024 point FFT analysis at 1-s interval. If data loss has occurred for some reason (e.g., CPU overloaded or data communication error), the time-synchronized observation fails.

We developed a synchronized observation system between the two CPUs by using the shared-packet exchanges as shown in Fig. 4. The two CPUs (CPU #8 and #9) are connected by the space wire protocol (as shown in Fig. 1) and can exchange a limited data packet ('shared-packet') every specified interval. The two CPUs have an individual reference time to collect a specific data packet and compare the current reference time and a time tag attached on a data packet observed by the EWO receiver. They process a data packet that has a time tag after the current reference time. They input the current reference time (TI + S-WPIA counter) onto a shared packet every 4 s. The CPU #8 compares reference times of each CPU and inputs new reference time onto a shared packet and set ups a flag to move to the synchronization mode if the two reference times are different. The two CPUs start processing of data packets that have time tags after the new reference time; then, simultaneous observation of electric and magnetic fields is enabled.

Matsuda *et al. Earth, Planets and Space* (2018) 70:75

Page 6 of 22

Fig. 3 A schematic diagram of the signal buffers on the each CPU

Fig. 4 A flowchart of the synchronized observation system

Onboard Frequency Analyzer

The OFA is one of the receivers of the PWE onboard the Arase satellite. The purposes of the OFA measurements are to obtain entire ELF/VLF plasma waves' activity and providing some properties (power spectrum, propagation direction, and polarization) for the wave mode determination. Particularly, the following plasma wave phenomena are the important targets of the OFA measurement: the chorus wave and the magnetosonic wave that are suggested to be drivers of the acceleration of relativistic electrons in the radiation belts, and the EMIC wave which is responsible for the scattering of relativistic electrons by anomalous cyclotron resonance. We use the data measured by the OFA to select specific events observed by the WFC. The OFA processes signals

detected by several dipole wire-probe antennas (WPT-S) (Kasaba et al. 2017) and tri-axis magnetic search coils (MSC) (Ozaki et al. 2018) installed onboard the satellite. Figure 5 shows the geometric configuration of the sensors. The OFA analyzes two components of electric fields (E_u and E_v) and three components of magnetic fields (B_α, B_β, and B_γ). The OFA performs fast Fourier transform (FFT) on the observed waveforms. The frequency range of electric field spectra is from DC to 20 or 130 kHz, and that of magnetic field spectra is a few Hz to 7 or 20 kHz. The WFC receiver can change its sampling rate and the threshold of the anti-aliasing filter. The maximum frequency of the observed spectra (f_{max}) changes depending on these settings (shown in Table 3). The '65.536 kHz (LF; low frequency) sampling rate and 20 kHz anti-aliasing filter's threshold mode' is the nominal mode for both electric and magnetic field measurements. The OFA measures the electric and magnetic field spectra up to 20 kHz in the nominal case. The '262.144 kHz (MF; middle frequency) sampling rate and 120 kHz anti-aliasing filter's threshold mode' is a redundant mode for the UHR frequency determination. The '16.384 kHz (VLF; very low frequency) sampling rate and 7 kHz anti-aliasing filter's threshold mode' is a special mode for the measurement of the low-frequency phenomena.

For the data amount reduction, the OFA uses a pseudo-logarithm frequency table, in which the frequency bands are divided into a linear frequency range and a logarithmic frequency range, in order to measure the characteristics of various plasma waves in a wide-frequency band. The kth ($k = 0, 1, 2, \ldots, p_f - 1$) element of the divided frequency array corresponds to the $n(k)$th element of the original frequency array:

$$n_1(k) = k(s + 1) + 1 \tag{1}$$

Matsuda *et al. Earth, Planets and Space* (2018) 70:75

Page 7 of 22
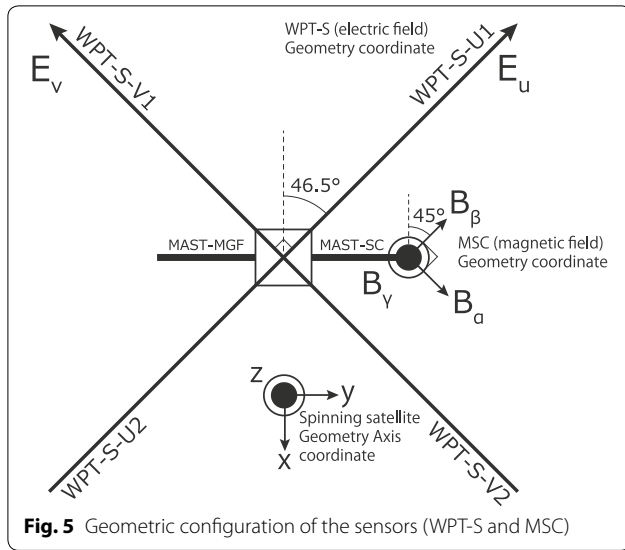
Fig. 5 Geometric configuration of the sensors (WPT-S and MSC)

Table 3 Variation of the maximum frequency of spectra observed by the OFA

Component	Sampling rate	LPF threshold (kHz)	f_{max} (kHz)
Electric field	LF (65.536 kHz)	20	20
		120	20
	MF (262.144 kHz)	20	20
		120	130
Magnetic field	LF (65.536 kHz)	20	20
	VLF (16.384 kHz)	7	7

$$n_2(k) = 10^{\frac{k}{N-1} \log \frac{f_{max}}{\Delta f}} \tag{2}$$

$$n(k) = \begin{cases} n_1(k) & \text{if } n_1(k) \geq n_2(k), \\ n_2(k) & \text{otherwise,} \end{cases} \tag{3}$$

where N, f_{max}, and Δf denote the length of the original frequency array, the maximum frequency of the reduced spectrum, and the frequency resolution of the original spectrum, respectively. s denotes the decimation interval in the linear frequency range. The reduced spectra of the linear frequency range become identical with the original spectra, except for the DC component when $s = 0$. $n_1(k)$ and $n_2(k)$ correspond to the linear frequency range and the logarithmic frequency range, respectively. The pseudo-logarithm frequency table adopts the larger value of these two values. Figure 6a–d shows the relationships of an element number of the reduced frequency array and a corresponding frequency of the four operation modes of the OFA (shown in "Modes"). We reduce the

frequency resolution by relocating the original frequency spectrum according to the frequency table. We decide individually for each product on the method for choosing the representative value in the frequency bins defined by the frequency table (e.g., the average value or the largest value in the frequency bin).

Products

The OFA produces the following three science products: (1) a single-channel power spectrum for electric and magnetic fields (OFA-SPEC), (2) the spectral matrices for electric and magnetic fields (OFA-MATRIX), and (3) full-channel complex spectra for electric and magnetic fields (OFA-COMPLEX).

OFA-SPEC is the auto-spectra of a selected channel for the electric and the magnetic fields. The channel of OFA-SPEC can be changed using a command from E_u, E_v, and $E_u + E_v$ for electric field and B_α, B_β, B_γ, and $B_\alpha + B_\beta + B_\gamma$ for magnetic field. Each element of an OFA-SPEC is averaged within the frequency bins defined by the frequency table. The electric and magnetic field spectra observed by the OFA-SPEC are given using the following equations:
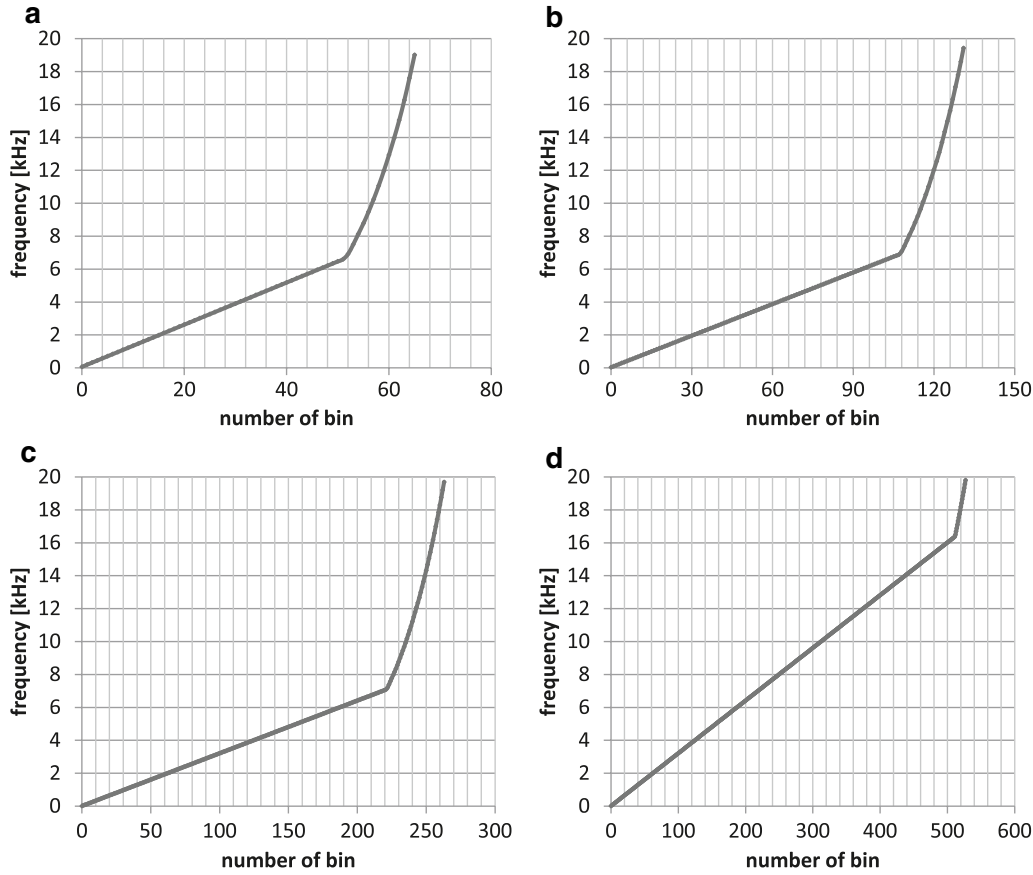
$$P_E(\omega) = \begin{cases} |E_u|^2 & (E_u \text{ mode}), \\ |E_v|^2 & (E_v \text{ mode}), \\ |E_u|^2 + |E_v|^2 & (E_u + E_v \text{ mode}), \end{cases} \tag{4}$$

$$P_B(\omega) = \begin{cases} |B_\alpha|^2 & (B_\alpha \text{ mode}), \\ |B_\beta|^2 & (B_\beta \text{ mode}), \\ |B_\gamma|^2 & (B_\gamma \text{ mode}), \\ |B_\alpha|^2 + |B_\beta|^2 + |B_\gamma|^2 & (B_\alpha + B_\beta + B_\gamma \text{ mode}). \end{cases} \tag{5}$$

The OFA-SPEC data are used as a survey data for the diagnostics of the plasma wave activity and for the selective downlink of the waveform observed by the WFC.

OFA-MATRIX is the variance–covariance matrix of the observed electric and magnetic field signals. Each element of an OFA-MATRIX is averaged within the frequency bins defined by the frequency table. Since the two CPUs individually produce electric and magnetic field spectral matrices, OFA-MATRIX does not measure any cross-spectra of an electric and magnetic field signal (e.g., $E_u B_\alpha^*$, $E_u B_\beta^*$, $E_u B_\gamma^*$, $E_v B_\alpha^*$, $E_v B_\beta^*$, $E_v B_\gamma^*$). The electric field matrix S_E and the magnetic field matrix S_B are given as follows:

$$S_E(\omega) = \frac{1}{4} \sum_{n=0}^{4} \begin{pmatrix} |E_u^{(n)}|^2 & E_u^{(n)} E_v^{(n)*} \\ E_v^{(n)} E_u^{(n)*} & |E_v^{(n)}|^2 \end{pmatrix}$$

$$= a_E \times \begin{pmatrix} s_{E00} & s_{E01} \\ s_{E10} & s_{E11} \end{pmatrix}, \tag{6}$$

Matsuda *et al. Earth, Planets and Space* (2018) 70:75

Page 8 of 22

Fig. 6 Onboard frequency tables of the OFA. **a** OFA_500MS mode, **b** OFA_1S mode, **c** OFA_2S mode, **d** OFA_4S mode

$$S_B(\omega) = \frac{1}{4} \sum_{n=0}^{4} \begin{pmatrix} |B_\alpha^{(n)}|^2 & B_\alpha^{(n)} B_\beta^{(n)*} & B_\alpha^{(n)} B_\gamma^{(n)*} \\ B_\beta^{(n)} B_\alpha^{(n)*} & |B_\beta^{(n)}|^2 & B_\beta^{(n)} B_\gamma^{(n)*} \\ B_\gamma^{(n)} B_\alpha^{(n)*} & B_\gamma^{(n)} B_\beta^{(n)*} & |B_\gamma^{(n)}|^2 \end{pmatrix}$$

$$= a_B \times \begin{pmatrix} s_{B00} & s_{B01} & s_{B02} \\ s_{B10} & s_{B11} & s_{B12} \\ s_{B20} & s_{B21} & s_{B22} \end{pmatrix}, \qquad (7)$$

where $E_i|_{i=u,v}$ and $B_j|_{j=\alpha,\beta,\gamma}$ is the electric and the magnetic Fourier spectra of the observed time-series signals, respectively. a_E and a_B are the normalization factors of the matrices and are always up to 1. The telemetry includes only the normalization factors, the real part of the diagonal component, and the real and imaginary parts of the upper triangular component. In order to guarantee statistical significance, the OFA-MATRIX is calculated independently from four consecutive FFT frames and their ensemble average is adopted. The OFA-MATRIX data are used for the direction finding and polarization analyses of the observed plasma waves. Since OFA-MATRIX has no correlation element between electric and magnetic fields, a propagation direction estimated from an OFA-MATRIX has ambiguity of its polarity.

OFA-COMPLEX is the complex spectra calculated using the FFT of the observed waveforms. The complex spectra for all five components are always generated simultaneously. The largest amplitude component within each frequency bin as defined by the frequency table is adopted for each element of the OFA-COMPLEX. We can calculate a Poynting flux and determine an absolute direction of a plasma waves by using a pair of an OFA-MATRIX data and an OFA-COMPLEX data.

The relationships between OFA-SPEC, MATRIX, and COMPLEX are shown in Fig. 7. The OFA-SPEC and OFA-COMPLEX are calculated from the first FFT frame used for calculating the OFA-MATRIX.

Modes

Table 4 shows the specifications of the four operation modes of the OFA. The generation time interval Δt of the OFA-SPEC can be selected from 0.5, 1, 2, and 4 s using
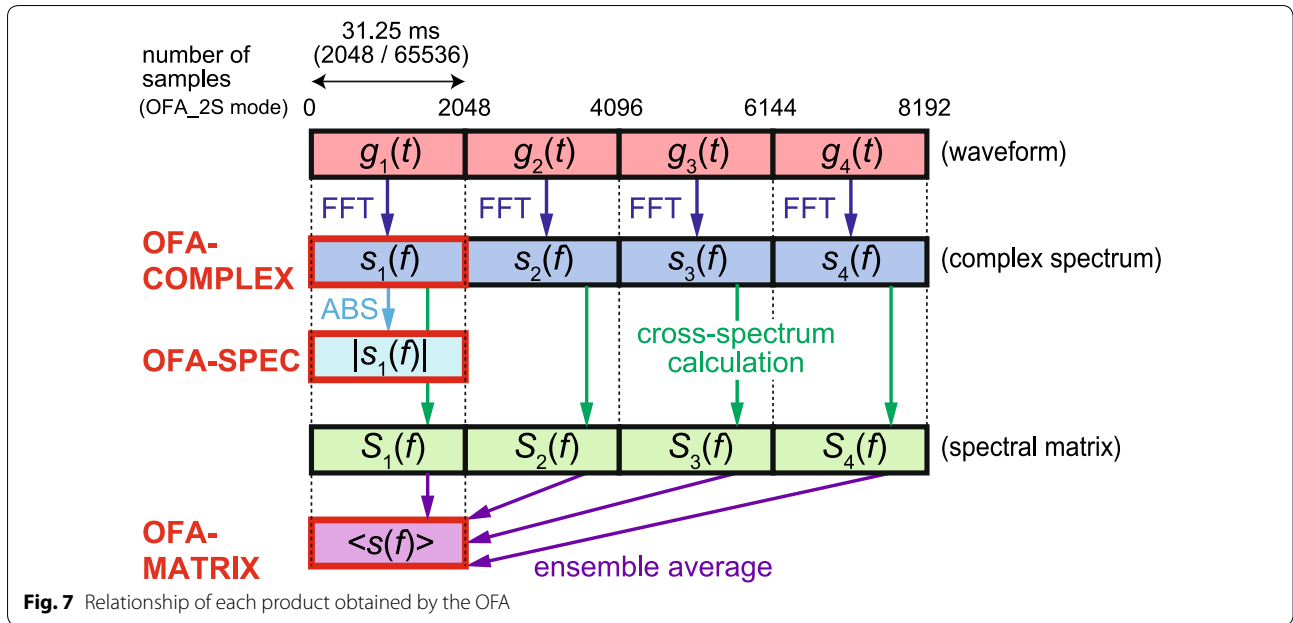
Matsuda *et al. Earth, Planets and Space* (2018) 70:75

Page 9 of 22

Fig. 7 Relationship of each product obtained by the OFA

Table 4 Generation time intervals Δt and the numbers of frequency points p_f in the four operation modes of the OFA

	OFA_500MS		OFA_1S		OFA_2S		OFA_4S	
	512p FFT		1024p FFT		2048p FFT		2048p FFT	
	Δt (s)	p_f (pts)	Δt (s)	p_f (pts)	Δt(s)	p_f (pts)	Δt (s)	p_f (pts)
Nominal								
OFA-SPEC	0.5	66	1	132	2	264	4	528
OFA-MATRIX	4		8		16		32	
OFA-COMPLEX	4		8		16		32	
Low-res								
OFA_SPEC	1	66	2	132	4	264	8	528
OFA-MATRIX	8		16		32		64	
OFA-COMPLEX	8		16		32		64	

a command, and the OFA-MATRIX and OFA-COMPLEX are generated at 8 times the time interval Δt. OFA changes the number of frequency points p_f between 66, 132, 264, and 528 points depending on the time interval Δt. The total data amount of the OFA does not change as the generation time interval changes because $(1/\Delta t) \cdot p_f$ is always constant. OFA changes the amount of data used for FFT analyses depending on the settings of the time interval Δt. For low bit-rate operation, 'low-resolution mode' doubles the generation time interval Δt while maintaining the number of frequency points p_f.

The data amount of OFA-SPEC, MATRIX, and COMPLEX in the OFA_1S (nominal) mode are follows:

- OFA-SPEC

  - Electric field: 1 (Hz) $\times$ 132 (pts) $\times$ 1 (channels) $\times$ 8 (bits) = 1056 bit,
  - Magnetic field: 1 (Hz) $\times$ 132 (pts) $\times$ 1 (channels) $\times$ 8 (bits) = 1056 bit,
- OFA-MATRIX

  - Electric field: {0.125 (Hz) $\times$ 132 (pts) $\times$ 16 (bits) + 32 (bits)} $\times$ 4 (elements) = 1184 bit,
  - Magnetic field: {0.125 (Hz) $\times$ 132 (pts) $\times$ 16 (bits) + 32 (bits)} $\times$ 9 (elements) = 2664 bit,
- OFA-COMPLEX

Matsuda *et al. Earth, Planets and Space* (2018) 70:75

Page 10 of 22

- Electric field: 0.125 (Hz) × 132 (pts) × 4 (elements) × 16 (bits) = 1056 bit,
- Magnetic field: 0.125 (Hz) × 132 (pts) × 6 (elements) × 16 (bits) = 1584 bit.

Waveform Capture

The WFC measures the electric and magnetic field waveforms. All the components of E_u, E_v, B_α, B_β, and B_γ are nominally obtained by the WFC. The component measured by the WFC can be changed using commands for the purpose of emphasized observation of specific components and to reduce the processing time. We perform the synchronized observation of electric and magnetic field waveforms by the shared-packet exchange between the two CPUs. One CPU decides and sends the start time of a burst operation to the other CPU. Each CPU monitors generated time of data packets from the EWO receiver and starts burst operation when the target packet comes from the receiver.

Modes and performance

The typical frequency range of whistler-mode chorus waves generated in the equatorial region is 0.1–0.8f_{ce} and correspond to a range from several hundred Hz to several dozen kHz in the inner magnetosphere, where f_{ce} denotes the local electron cyclotron frequency (Santolík et al. 2003b, 2004; Tsurutani and Smith 1974). On the other hand, EMIC waves are detected below the local proton cyclotron frequency (f_{cH+}) and corresponds to a range from a few Hz to several hundred Hz in the inner magnetosphere (Gendrin et al. 1984; Gomberoff and Neira 1983; Mauk 1982). Since the frequency ranges of the targets are different, we installed two operation modes: 'chorus burst mode' and 'EMIC burst mode.'
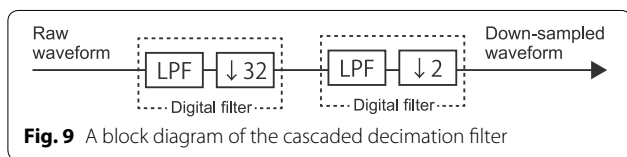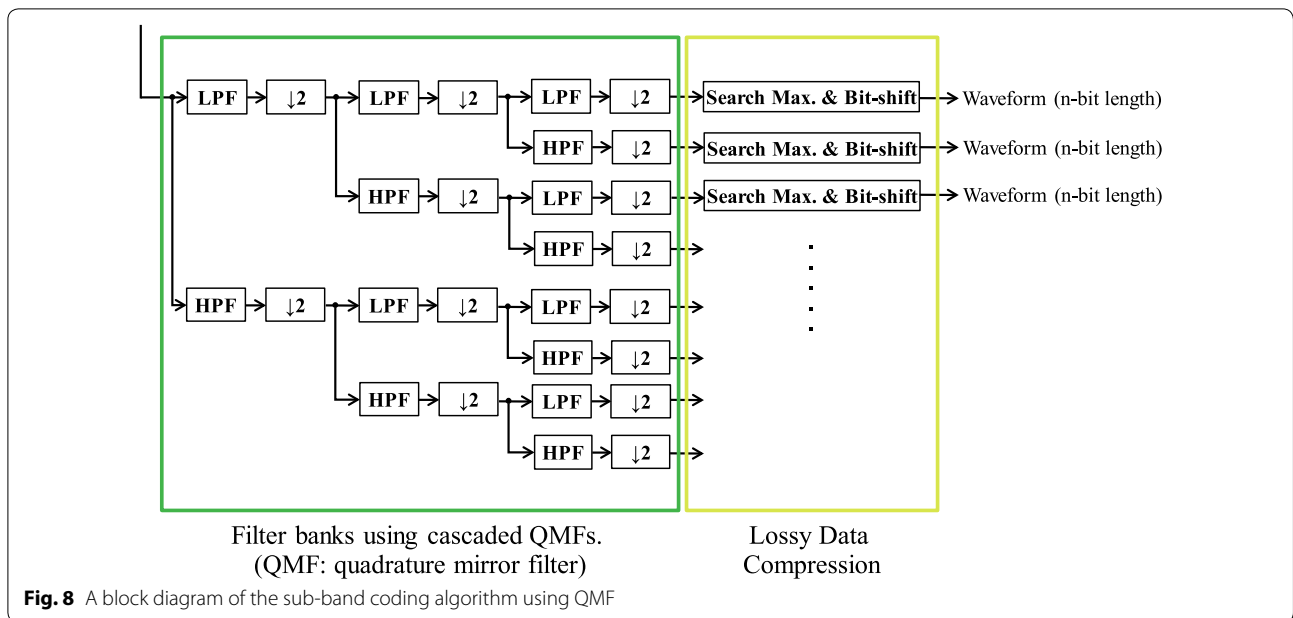
Chorus burst mode measures electric and magnetic field waveform data at a high sampling rate (65,536 samples/s). This mode is designed for the wide-frequency range measurement of whistler-mode chorus emission, plasmaspheric hiss, and electron cyclotron harmonic waves. In order to reduce the data amount, waveform obtained using the 'chorus burst mode' is encoded by the sub-band coding algorithm into 8 bands for every 8192 points (Hashimoto et al. 2003). Figure 8 shows a block diagram of the algorithm. We used 8 taps quadrature mirror filter (QMF)-tree filter bank. After divided into 8 bands, we calculate a maximum sample in each sub-band and reduce bit length of the samples. The data amount is reduced to approximately 55% of the original data amount by the compression. In the chorus burst mode, we nominally apply the data compression process described above. On the other hand, we can select uncompressed mode for the purpose of short-interval burst operation although the data amount almost doubles.

The EMIC burst mode measures electric and magnetic field waveform data at a low sampling rate (1024 samples/s). This mode is designed for the measurements of low-frequency phenomena such as EMIC waves and magnetosonic waves. It is well known that magnetosonic waves exhibit clear harmonic structures at multiples of the proton cyclotron frequency at generation regions (Kasahara et al. 1994; Perraut et al. 1982; Walker et al. 2015). Since the proton cyclotron frequency along the orbit of Arase is typically below 300 Hz, EMIC burst mode is sufficient for the magnetosonic wave measurement. The amount of data is 1/64 of chorus burst-mode waveform, and hence, we can obtain waveforms for long periods. This is enabled by the down-sampling technique realized by a combination of decimation filters. We perform 1/64 decimation of observed waveforms by using the cascaded decimation filter as shown in Fig. 9. Figures 10 and 11 show frequency responses of the anti-aliasing filters for the 1/32 decimation filter (150 taps) and that for the 1/2 decimation filter (31 taps), respectively. The normalized cutoff frequencies of each filter are 0.015625 (the normalized Nyquist frequency of 1/32) and 0.25 (the normalized Nyquist frequency of 1/2), respectively. These filters have nearly linear phase responses for almost entire Nyquist frequency range.
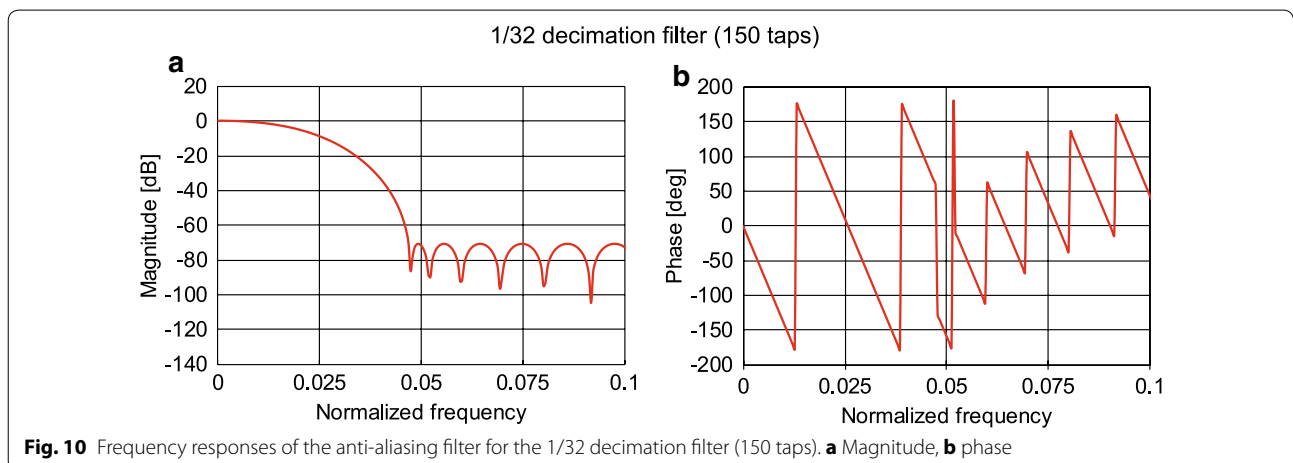
The EFD burst mode (Kasaba et al. 2017) is simultaneously operated, while chorus (EMIC) burst mode is operating. 'Chorus burst mode' and 'EMIC burst mode' operate exclusively. We operate 'chorus burst mode' and 'EMIC burst mode' when the apogee of the Arase satellite is located in the post-midnight sector (chorus wave generation region) and in the dusk sector (EMIC wave generation region) of the nominal plan, respectively. The length of the continuous waveforms obtained by the WFC can be changed with a command to a ceiling of up to 200 s. The number of repeat observation and time interval can also be changed with a command.
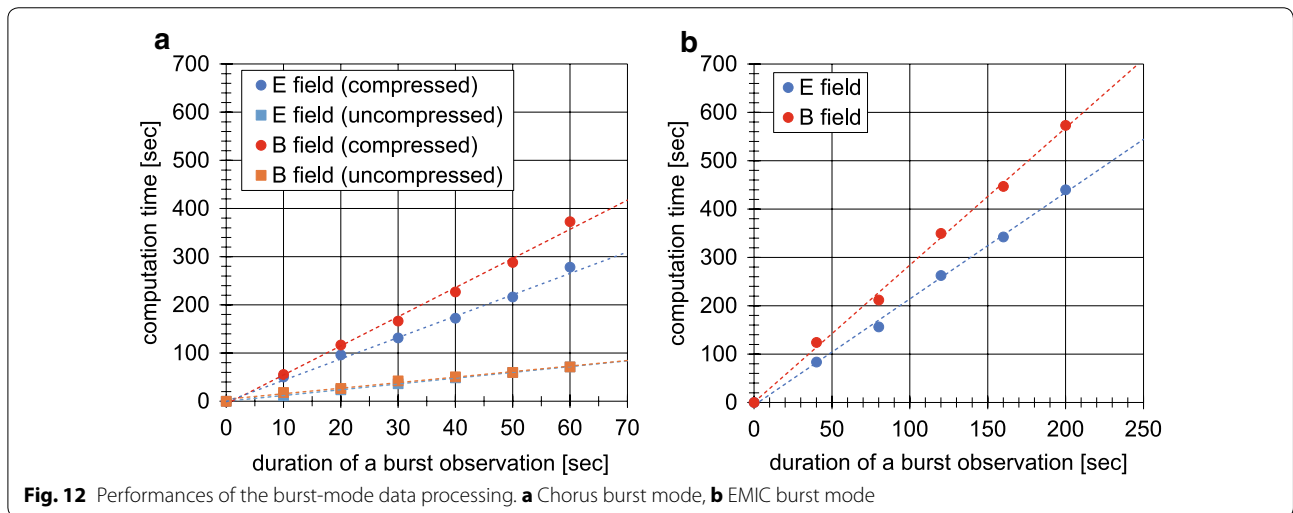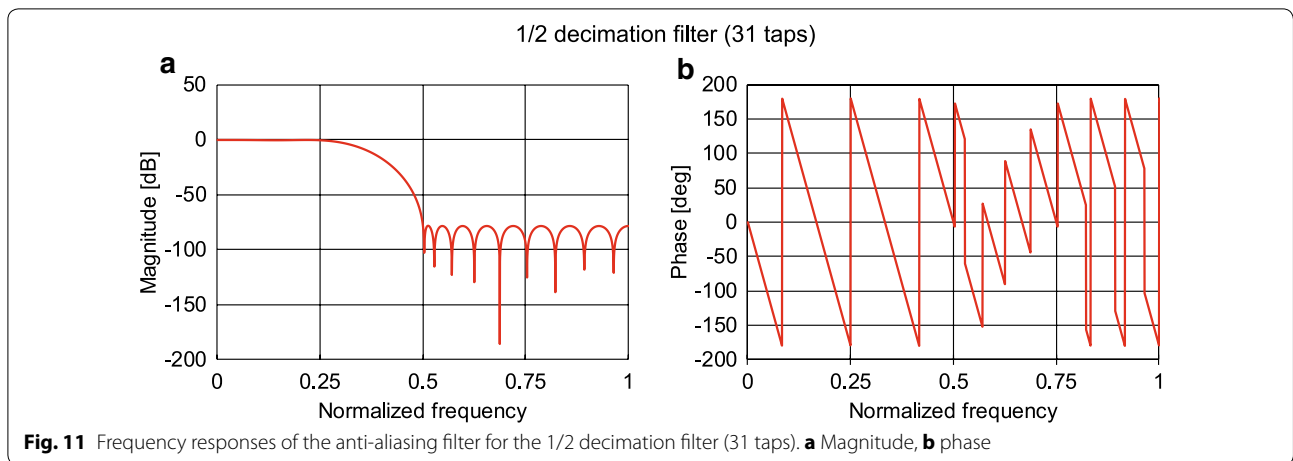
Figure 12a, b represents the relationships between the length of a one-shot waveform and the computation time for chorus burst mode and EMIC burst mode. Because the generation of the burst-mode data is a time-consuming process, we first freeze the long buffer to keep the data for the burst data generation (see "Signal buffers"). Then, new observation data are stored in the short buffer and continuous data are generated using the data in the short buffer, while burst data are processed as a background process. After the processing finished, the destination of new observation data is changed to the long buffer. Consequently, we have to wait for finish running the computation before we activate additional

Matsuda *et al. Earth, Planets and Space* (2018) 70:75

Page 11 of 22

Fig. 8 A block diagram of the sub-band coding algorithm using QMF

Fig. 9 A block diagram of the cascaded decimation filter

burst operation. For both modes, the computation time increases in proportion to the length of the waveform and is almost 5 times the measured waveform duration. The computation time of compressed chorus burst mode is approximately 4.6 times and 6.3 times the duration of a burst observation for an electric field waveform (E_u and E_v) and a magnetic field waveform (B_α, B_β, and B_γ),

respectively (red and blue circles in Fig. 12a). The computation time for magnetic field waveforms is approximately 1.4 times that for electric field waveforms since the data amount for magnetic field waveforms with three axes is larger than that of electric field waveforms with two axes. The computation time for uncompressed chorus burst mode is approximately 1.4 times that of the duration of a burst observation for electric and magnetic field waveforms (red and blue rectangles in Fig. 12a). The computation times for electric and magnetic field waveforms are almost the same since each CPU has a few processing tasks for generating uncompressed waveforms. The computation time for EMIC burst mode is approximately 2.2 times and 2.9 times that of the duration of a burst

Fig. 10 Frequency responses of the anti-aliasing filter for the 1/32 decimation filter (150 taps). **a** Magnitude, **b** phase

Matsuda *et al. Earth, Planets and Space* (2018) 70:75

Page 12 of 22

Fig. 11 Frequency responses of the anti-aliasing filter for the 1/2 decimation filter (31 taps). **a** Magnitude, **b** phase

Fig. 12 Performances of the burst-mode data processing. **a** Chorus burst mode, **b** EMIC burst mode

observation for electric and magnetic field waveforms, respectively (red and blue circles in Fig. 12b). When we perform a cyclic burst observation, we require additional time (almost the same as the duration of the burst observation) for the waveform data to be stored into the long buffer (see the previous section).

The data amount of 1 s waveform observed by 'chorus burst mode' and 'EMIC burst mode' are follows:

- Chorus burst mode

  - Electric field: 65,536 (samples) × 2 (channels) × 16 (bits) × 0.55 = 1.15 Mbit,
  - Magnetic field: 65,536 (samples) × 3 (channels) × 16 (bits) × 0.55 = 1.73 Mbit,

- EMIC burst mode

  - Electric field: 1024 (samples) × 2 (channels) × 16 (bits) = 32 kbit,
  - Magnetic field: 1024 (samples) × 3 (channels) × 16 (bits) = 49 kbit.

Data storage

The burst data will be stored once on the mission data recorder (MDR) and downloaded to the ground after data selection using the continuous data obtained by the OFA. The MDR has each four partitions for 'chorus burst mode' and 'EMIC burst mode'. The two partitions of the chorus burst mode (chorus-E 1 and chorus-E 2) are for electric field waveforms, and the other two partitions

Matsuda *et al. Earth, Planets and Space* (2018) 70:75

Page 13 of 22

Table 5 The configuration of the MDR partition

Partition	Size (Gbytes)
Category1	
Chorus-E 1	1.6
Chorus-B 1	2.4
EMIC-E 1	0.8
EMIC-B 1	1.2
EFD 1	0.6
Category2	
Chorus-E 2	1.6
Chorus-B 2	2.4
EMIC-E 2	0.8
EMIC-B 2	1.2
EFD 2	0.6

Table 6 A list of auto-triggering conditions for burst-mode operation

Receiver	Data type		Remarks
EFD	SC potential		
	Spectrum	1–3 Hz	EMIC & MSW
		3–10 Hz	EMIC & MSW
		10–32 Hz	EMIC & MSW
		32–100 Hz	EMIC & MSW
		100–224 Hz	EMIC & MSW
OFA	Spectrum (electric field)	DC–f_c/45	EMIC
		f_c/45–f_c/4	MSW
		f_c/10–f_c/2	Lower band chorus, hiss
		f_c/2–f_c	Upper band chorus
		f_c–5f_c	ECH
	Spectrum (magnetic field)	DC-f_c/45	EMIC
		f_c/45–f_c/4	MSW
		f_c/10–f_c/2	Lower band chorus, hiss
		f_c/2–f_c	Upper band chorus
		f_c–5f_c	
HFA	Plasma frequency		
(MGF)	Cyclotron frequency		

(chorus-B 1 and chorus-B 2) are for magnetic field waveforms. Likewise, the two partitions of the EMIC burst mode (EMIC-E 1 and EMIC-E 2) are for electric field waveforms and the other two partitions (EMIC-B 1 and EMIC-B 2) are for magnetic field waveforms. All channels for electric (magnetic) field waveforms are stored into one category. The size of each partition is shown in Table 5.

We define a 'category' as a combination of one partition for electric field waveforms and another for magnetic field waveforms. The chorus (EMIC) burst data can be stored on a selected category by the telemetry command. Nominally, we use one of these two categories as 'write category' and use the other one as 'read category', and we rotate their roles every several days. Thus, we keep observed burst data on the one category during several days for the selective downlink.

When the WFC measures all the components (E_u, E_v, B_α, B_β, and B_γ), 185 min of chorus burst waveforms and 55 h of EMIC burst waveforms can be stored into one category. The information from burst-mode operation (start time, end time, duration, and category) is recorded as supplementary data for the WFC.

Triggering
Since the size of each MDR category is finite, we cannot store 100% of waveform data. We intermittently activate burst mode using timeline execution with commands or auto-triggering performed by the onboard processor. The parameters of the burst operation command are follows: (1) the number of cycles, (2) cyclic interval, (3) start time, and (4) duration. If we set the number of cycles to be infinite, burst observation continues at a specified interval until a burst-stop command is received. If a burst-stop command is not received before a MDR category fills up, the earliest data will be overwritten.

The activation condition of the onboard auto-trigger can be chosen from the values shown in Table 6. The power spectrum of OFA-SPEC is divided into 5 bands using the electron cyclotron frequency calculated from the DC magnetic field obtained by the magnetic field experiment (MGF) instruments (Matsuoka et al. 2017). The intensities of the divided bands are calculated as the maximum intensity of the several frequency bins. When the calculated electron cyclotron frequency exceeds 6553.6 Hz, we set the reference frequency used for band division to 6553.6 Hz. Each band corresponds to the typical frequency of major plasma waves in the inner magnetosphere. The trigger data are updated every 4 s and hold the peak value until being reset at a fixed time.

Onboard SoftWare CALibration function
Principle
The SWCAL function is a function of the onboard software of WFC/OFA used for measuring the transfer functions of the receiver and the electric field's antenna impedance. The EWO receiver divides its FPGA base-clock (16.777216 MHz) and generates a square waveform with an arbitrary frequency as a calibration signal. The SWCAL function changes the division ratio of the FPGA base-clock stepwise using software control and inputs the calibration signals of various frequencies to the input stage of the preamplifier. The function acquires its complex spectra $f(\omega)$ using FFTs. On the other hand,

Matsuda *et al. Earth, Planets and Space* (2018) 70:75

Page 14 of 22

on the ground, we generate a square wave identical to the calibration signal and calculate its Fourier transform $g(\omega)$. The transfer function of the receiver $H(\omega)$ can be obtained using the following ground processing equation:

$$H(\omega) = f(\omega)/g(\omega). \tag{8}$$

The square wave has components at the fundamental frequency and its odd harmonic frequency, and the harmonic component gradually attenuates at 6 dB/oct. We can calculate the transfer function not only at fundamental frequencies but also at the odd multiple frequencies. The step of the calibration signal used by the SWCAL function is specified with following three parameters: (1) initial frequency, (2) number of steps, and (3) step mode (linear or exponential). For example, if the initial frequency is 32 Hz, the number of steps is 5. Then, in the exponential step mode, square waves of 32, 64, 128, 256, and 512 Hz are sequentially outputted and responses are acquired. In the case of the linear step mode, rectangular waves of 32, 64, 96, 128, and 160 Hz are sequentially outputted with the same initial frequency and step number and responses are acquired. We can select an operation mode of the SWCAL function from the following modes:

ODD mode   The function acquires the components only at a fundamental frequency and at the odd harmonic frequencies of the frequency spectrum of the calibration signal.

ALL mode   The function acquires all components of the frequency spectrum of the calibration.

RAW mode   The function acquires the raw waveform of the calibration signal (the first 2048 points).
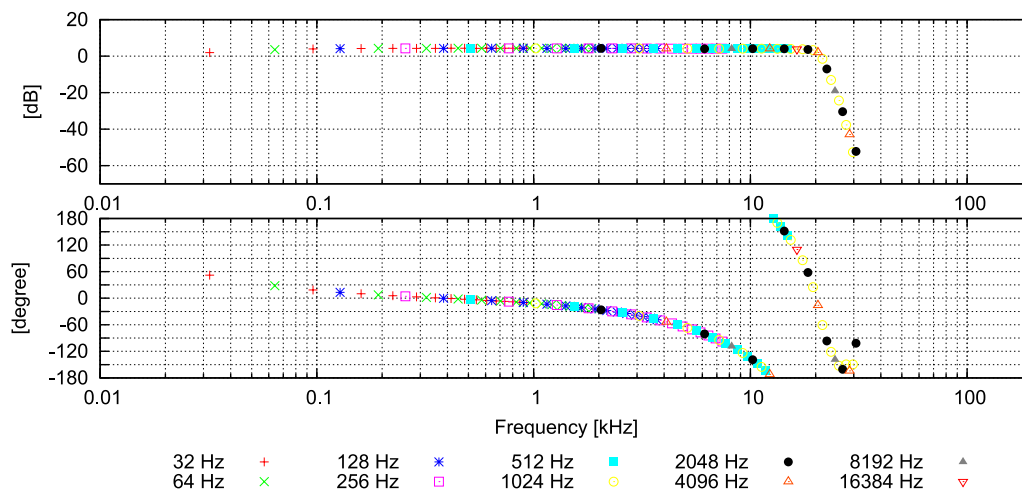
Test on the ground

For the test of the onboard calibration technique, we fed calibration signals into the input of the WPT-PRE(AC) and performed SWCAL procedure. We obtained complex spectra at the fundamental frequency and the odd (up to the 29th order) harmonic frequencies of the square waves (source calibration signals). Then, we calculated the frequency response of the receiver by calculating Eq. (8). Figure 13 shows the pre-launch results of the SWCAL function. (The top and bottom panels show the amplitude and phase characteristics, respectively.) Each mark in Fig. 13 represents calculated frequency response by using each source calibration signal (initial frequency = 32 Hz, number of steps = 10, exponential step mode). The calculated frequency responses correspond reasonably well with the experimental data (not shown here).

Measurement of antenna impedance

Figure 14 shows a simplified schematic diagram of the calibration signal input at the WPT-PRE(AC) [the detailed circuit is shown in Kasahara et al. (2018)]. The diagram also contains the antenna impedance of the WPT-S. For the purpose of simplicity, we assume the parallel circuit as the antenna impedance, which consists of the typical plasma impedance of 10 MΩ and the theoretical capacitance of 70 pF for the WPT-S in vacuum. The calibration signal is fed into the input of the WPT-PRE(AC) through the selectable specific impedance(R_{CAL}). The input circuit is dedicated to the comprehensive calibration of the WPT-PRE(AC) and WFC(E) as well as the measurement of antenna impedance.

We can select the changeable impedance by the telemetry command among 1 kΩ, 100 kΩ, 1 MΩ, and 10 MΩ. The calibration signal is affected by the relation of the selected resistance and the antenna impedance. Figure 15

Fig. 13 A sample result of the SWCAL function obtained on the ground

Matsuda *et al. Earth, Planets and Space* (2018) 70:75

Page 15 of 22
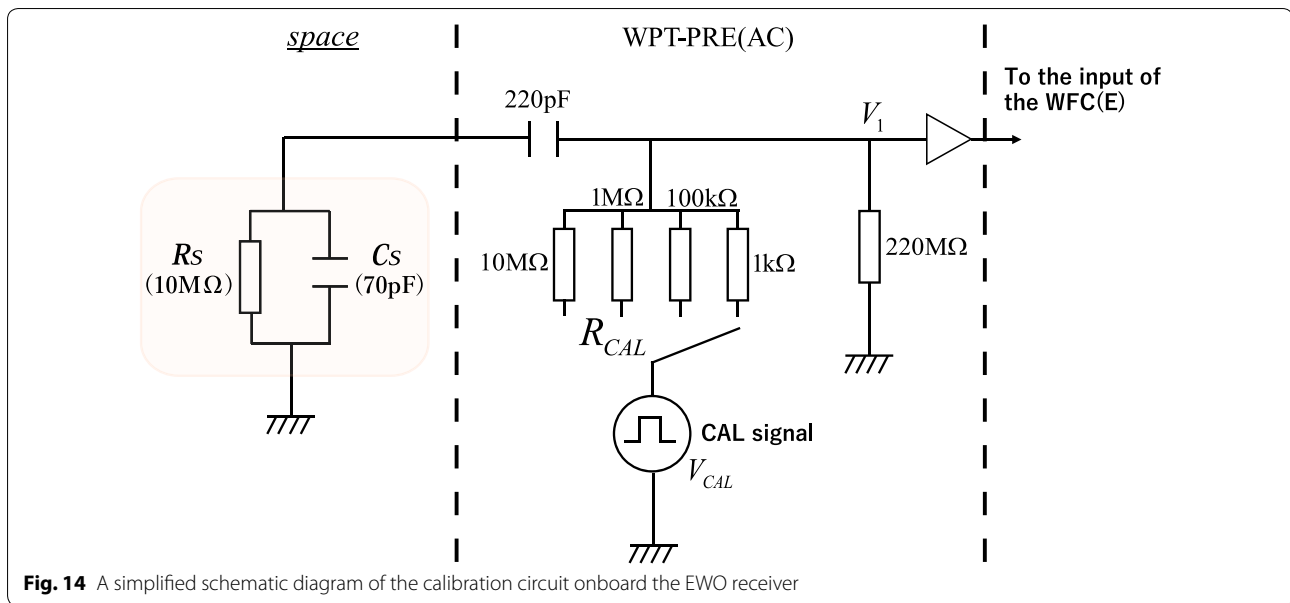
Fig. 14 A simplified schematic diagram of the calibration circuit onboard the EWO receiver
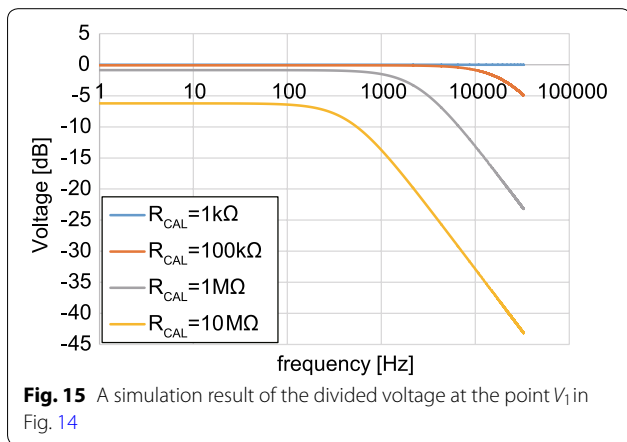
Fig. 15 A simulation result of the divided voltage at the point V_1 in Fig. 14

shows the simulation result of the divided voltage at the point V_1 in Fig. 14. Since the effect of the antenna impedance is ignored when R_{CAL} is selected to $1\,\text{k}\Omega$, we can measure the end-to-end frequency response of the WFC receiver including the preamplifier [see Kasahara et al. (2018) in this issue]. On the other hand, observed signals by the WFC receiver include effects of the antenna impedance when $R_{CAL} > 100\,\text{k}\Omega$. We can calculate R_S and C_S by solving simultaneous equations of the two frequency responses of the circuit (under the two different R_{CAL} values).

Other functions
Automatic gain control
The EWO receiver has programmable gain amplifiers (PGAs). We can select gains by telemetry commands from four (0, 20, 40, and 60 dB) for the electric field and from two (0 and 20 dB) for the magnetic field. We developed automatic gain control (AGC) system which performs automatic selection of appropriate gains for the electric and magnetic field measurements by monitoring peak values of instantaneous electric and magnetic field waveforms. The resolution of the A/D converters onboard the EWO receiver is 14 bit. We set the lower and higher thresholds at $128 = (1000\,0000)_2$ and $4096 = (1\,0000\,0000\,0000)_2$ A/D count value. If the level of instantaneous waveform becomes over the higher threshold level, the AGC system sends a telemetry command to switch to low gain. On the other hand, the level becomes less than the lower threshold level, the AGC system sends a telemetry command to switch to high gain. The AGC system obtains instantaneous waveforms and controls PGA gains every 7 spins. We can observe not only very weak events but also large amplitude events (e.g., large amplitude whistlers) by using the AGC system.

S-WPIA mode
When the PWE instrument receives a request for S-WPIA data generation from the mission data recorder (MDR), the WFC continuously generates and stores 5 components of the electric and magnetic field waveforms to the MDR. The chorus (EMIC) burst mode and this function are exclusively operated. That is, when the PWE instrument receives a request for S-WPIA mode operation during the generation of WFC data, the generation of WFC data is suspended and that of S-WPIA data is prioritized. After receiving a S-WPIA data stop request, the generation of WFC data is automatically resumed. During operation in S-WPIA

Matsuda *et al. Earth, Planets and Space* (2018) 70:75

Page 16 of 22

mode, a large amount of data is simultaneously sent to the MDR, and so the load of the mission telemetry processing performed by the middleware increases. When the telemetry processing queue of the middle ware becomes full, PWE stops transmitting data. It is restarted when the load returns to a moderate value. Since the observed data of the PWE is discarded while the transmission is stopped, the S-WPIA data of the MDR are not necessarily continuous.

Real-time telemetry

The onboard software of the PWE has a real-time operation mode for acquiring data that requires immediate attention, such as the extended operation of the WPT and MAST. In the real-time operation mode, the same data as those of OFA-SPEC are stored in the HK data packet at a cycle of once every 4 s. The number of frequency points p_f of the OFA-SPEC is synchronized with the relevant setting in the OFA.

Initial results

After Arase was launched on December 20, 2016, we deployed antennas (WPT-S and MSC) and started nominal operation. In order to confirm that our onboard software satisfies technical and scientific requirements, we show initial results obtained by the PWE.

The top panel of Fig. 16 shows the electric field spectra from 1 kHz to 1 MHz as observed by the HFA of the PWE on April 09, 2017. The middle and bottom panels of Fig. 16 show the power spectra of electric and magnetic fields during the day as measured by OFA-SPEC, respectively. The solid black line and dashed black line indicate the local electron cyclotron frequency (f_{ce}) and half of the local electron cyclotron frequency ($0.5f_{ce}$), respectively, as calculated from the DC magnetic field measurement by the MGF instrument onboard the Arase satellite. The configuration of the channel was absolute mode ($E_u + E_v$ and $B_\alpha + B_\beta + B_\gamma$ for the electric and the magnetic fields, respectively). Since 'OFA-1S mode' was used at this time, the time resolution and the number of frequency bins are 1 s and 132 points, respectively. We calibrated the electric field spectra under the assumption of the theoretical antenna capacitance in vacuum (70 pF), the typical plasma impedance (10 MΩ) and 15 m of the effective length of the WPT-S. Whistler-mode chorus waves were clearly observed around 0.2–4 kHz from 00:00 to 07:00 UT and from 10:00 to 15:30 UT. Gaps in the chorus waves were clearly observed at around half of the electron cyclotron frequency ($0.5f_{ce}$) from 02:00 to 03:30 UT and from 10:30 to 12:00 UT. Electrostatic electron cyclotron harmonic (ECH) waves were observed above f_{ce} when the Arase satellite crossed the geomagnetic equator
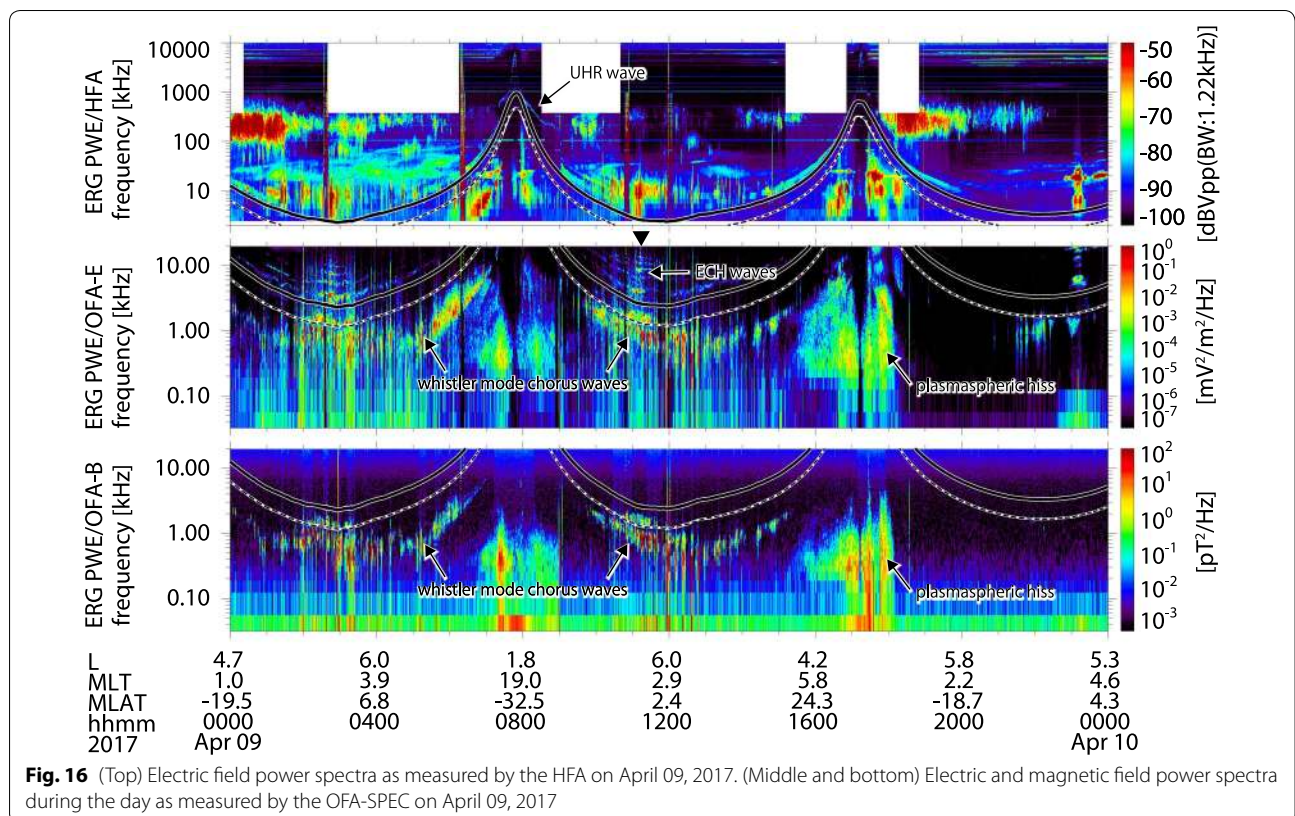
Fig. 16 (Top) Electric field power spectra as measured by the HFA on April 09, 2017. (Middle and bottom) Electric and magnetic field power spectra during the day as measured by the OFA-SPEC on April 09, 2017

Matsuda *et al. Earth, Planets and Space* (2018) 70:75

Page 17 of 22

(02:50, 11:23, and 23:22 UT). Sudden decreases in the upper hybrid resonance (UHR) frequency observed by the PWE/HFA indicate that the Arase satellite was in the plasmasphere from 07:20 to 09:00 UT and from 16:40 to 18:05 UT. Plasmaspheric hiss was observed below several kHz in these periods. Figure 17 shows an enlarged view of the observed spectra from 11:00 to 11:20 UT. We identified some chorus groups from the continuous OFA-SPEC data. Since the time resolution of OFA-SPEC is 1 s, a periodic feature shown in Fig. 17 does not correspond to the appearance of chorus elements. Even so, resolution of power spectra obtained by OFA-SPEC is sufficient to identify plasma waves.

Figure 18 shows an example of the wave propagation vector analyses using data obtained by OFA-MATRIX(B). Figure 18a–c represents the power spectra of B_x, B_y, and B_z components in the Spinning satellite Geometry Axis (SGA) coordinate, respectively (see Fig. 5). These are calculated by the coordinate transformation in the *xy*-plane of the diagonal components of the observed matrix. Figure 18d–f shows the wave normal angle direction, the ratio of the polarization ellipse (the pulse and minus signs indicate right- and left-handed polarization, respectively), and planarity as calculated using the singular value decomposition (SVD) method (Santolík et al. 2003a). We performed SVD after the transformation from the SGA coordinate to the ambient magnetic field aligned coordinate by using DC magnetic field measurement by the MGF instrument onboard Arase. The results indicate that the observed chorus emission propagates almost parallel ($\sim 10°$) along the geomagnetic field lines and that their polarizations are clearly right-handed.

Since the planarities of the observed waves are nearly at unity, the emissions are mostly plane waves.

Figure 19 shows the results of the waveform observation by the PWE/WFC in chorus burst mode from 11:10:54 to 11:11:24 UT on April 9, 2017 (black arrow in Figs. 16, 17, 18). Figure 19a–e shows the observed electric and magnetic field waveforms (E_u and E_v in the WPT-S (electric field) Geometry coordinate and B_α, B_β, and B_γ in the MSC (magnetic field) Geometry coordinate). Figure 19f–j shows the dynamic power spectra of the observed waveforms as calculated using short-time Fourier transform (STFT) analysis with a 62.5-ms Hann window that included 4096 samples with a 94% overlap (shifting the window by 256 samples). We observed rising-tone chorus wave elements with a gap at half the electron cyclotron frequency.

Figure 20 shows the results of the waveform observation by the PWE/WFC EMIC in burst mode from 08:01:05 to 08:01:55 UT on April 9, 2017 (red arrow in Figs. 16, 17, 18). Figure 20a–e shows the observed electric and magnetic field waveforms (E_u and E_v in the WPT-S (electric field) Geometry coordinate and B_α, B_β, and B_γ in the MSC (magnetic field) Geometry coordinate). We performed high-pass filtering with a cutoff at 1 Hz to remove the satellite spin tone. Figure 20f–j shows the dynamic power spectra of the observed waveforms as calculated using STFT analysis with a 500-ms Hann window that included 512 samples with a 12.5% overlap (shifting the window by 64 samples). We observed lightning whistler waves and lightning-induced EMIC waves (ion cyclotron whistlers) during this period. We can estimate the local cold ion composition using characteristic frequency
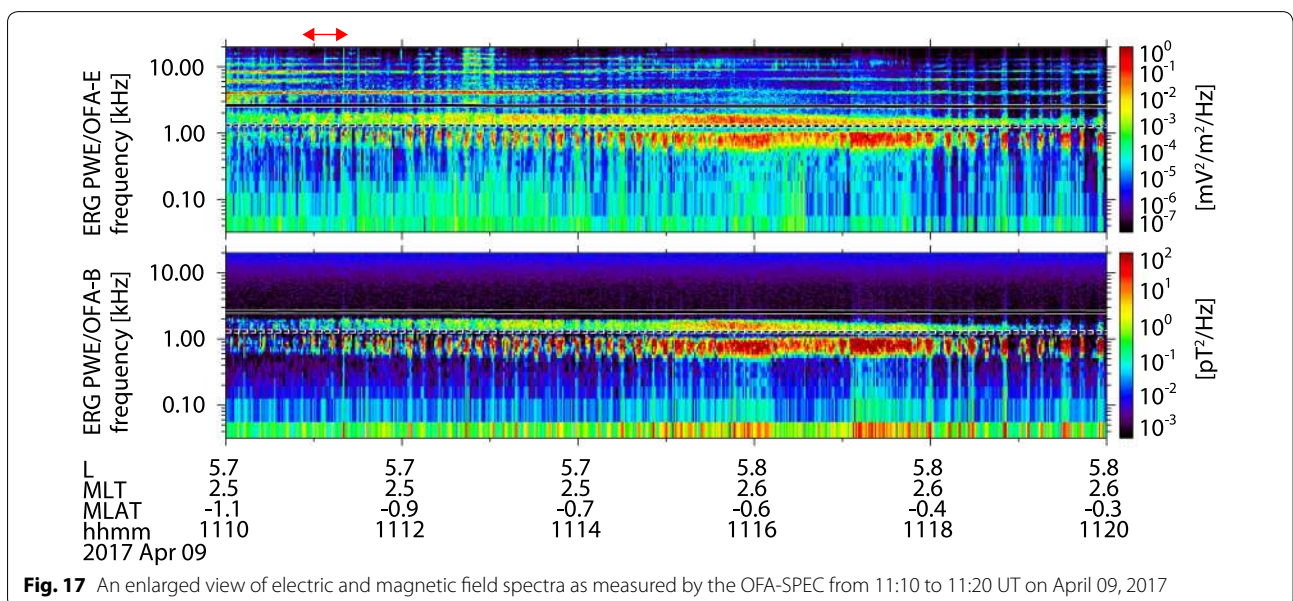
Fig. 17 An enlarged view of electric and magnetic field spectra as measured by the OFA-SPEC from 11:10 to 11:20 UT on April 09, 2017

Matsuda *et al. Earth, Planets and Space* (2018) 70:75

Page 18 of 22
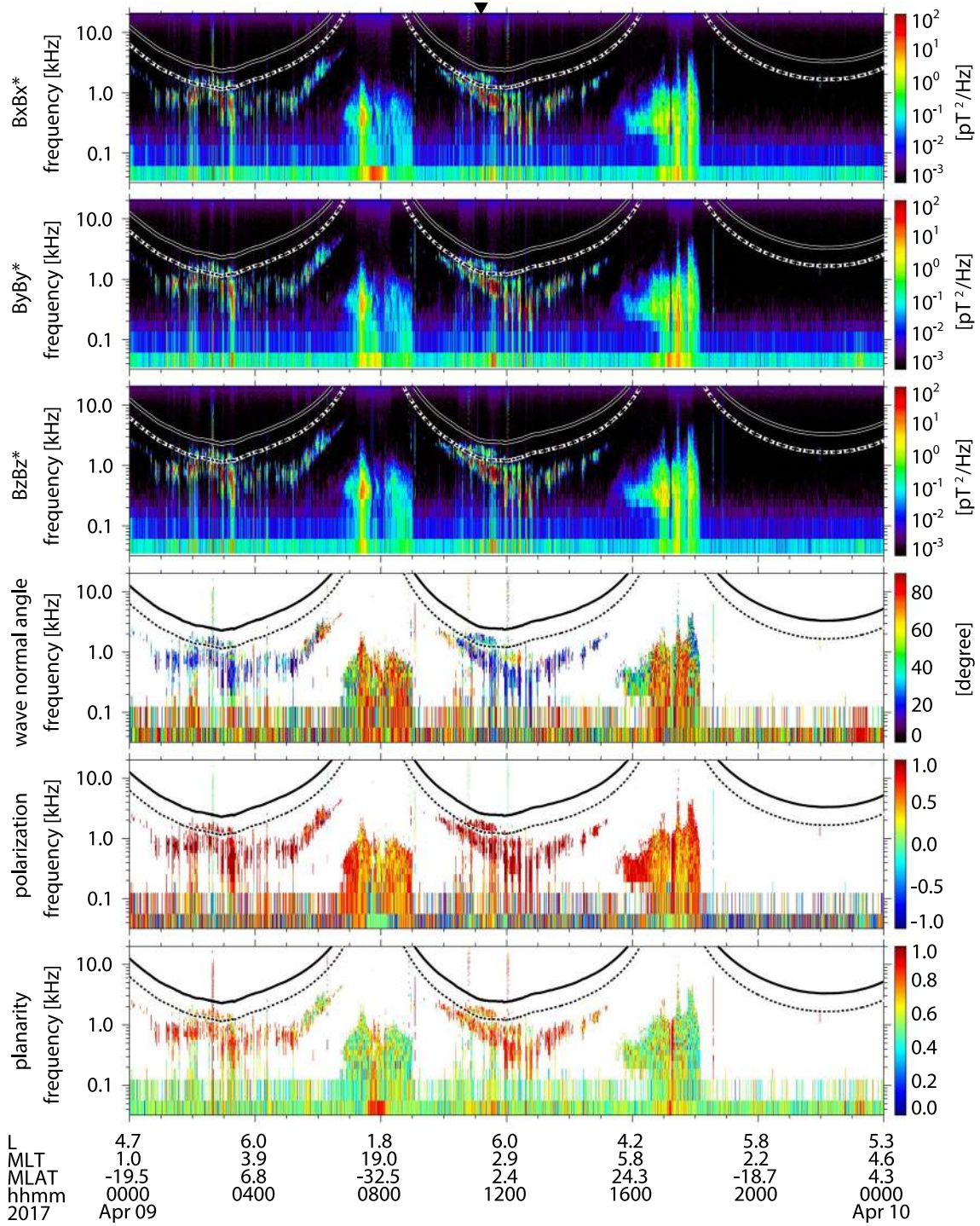
Fig. 18 An example of the wave propagation vector analyses by using data obtained by OFA-MATRIX(B) on April 09, 2017

Matsuda *et al. Earth, Planets and Space* (2018) 70:75

Page 19 of 22
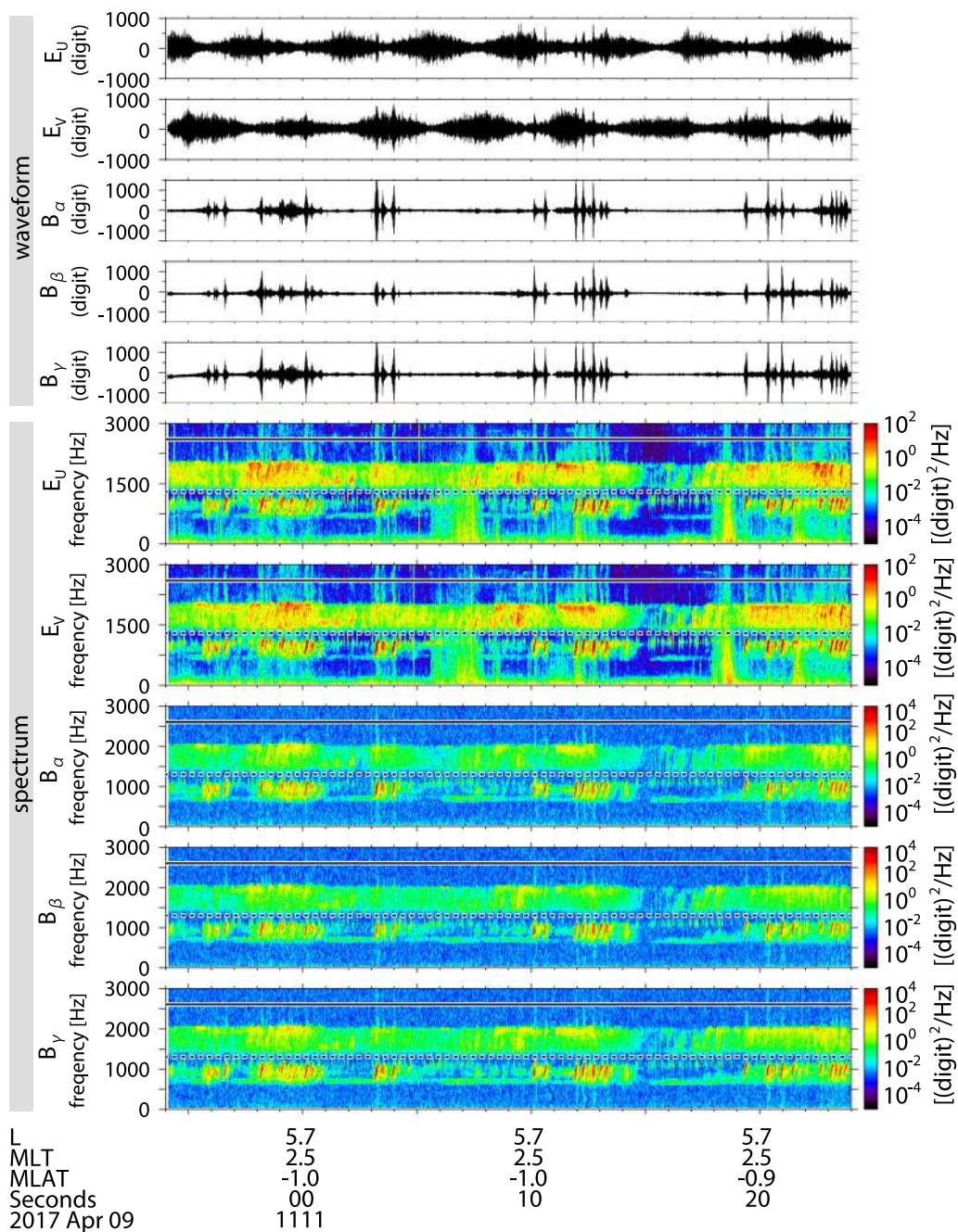
Fig. 19 A sample result of waveform observation by the PWE/WFC in chorus burst mode from 11:10:54 to 11:11:24 UT on April 9, 2017

analysis for ion cyclotron whistlers (Matsuda et al. 2014, 2015, 2016). The asymptotic frequency of the observed ion cyclotron whistler waves indicates the local proton cyclotron frequency.

Conclusion

We presented specifications of the onboard software of the PWE onboard the Arase satellite. We designed the onboard software to achieve the simultaneous observations of wide-band electric and magnetic field spectra and waveforms. Two CPUs onboard the PWE process electric field data and magnetic field data, respectively. We achieved time-synchronized measurements by using a shared-packet exchange between the two CPUs. The OFA successfully obtained electric and magnetic field power spectra every 0.5–4 s and spectral matrices and

Matsuda *et al. Earth, Planets and Space* (2018) 70:75

Page 20 of 22
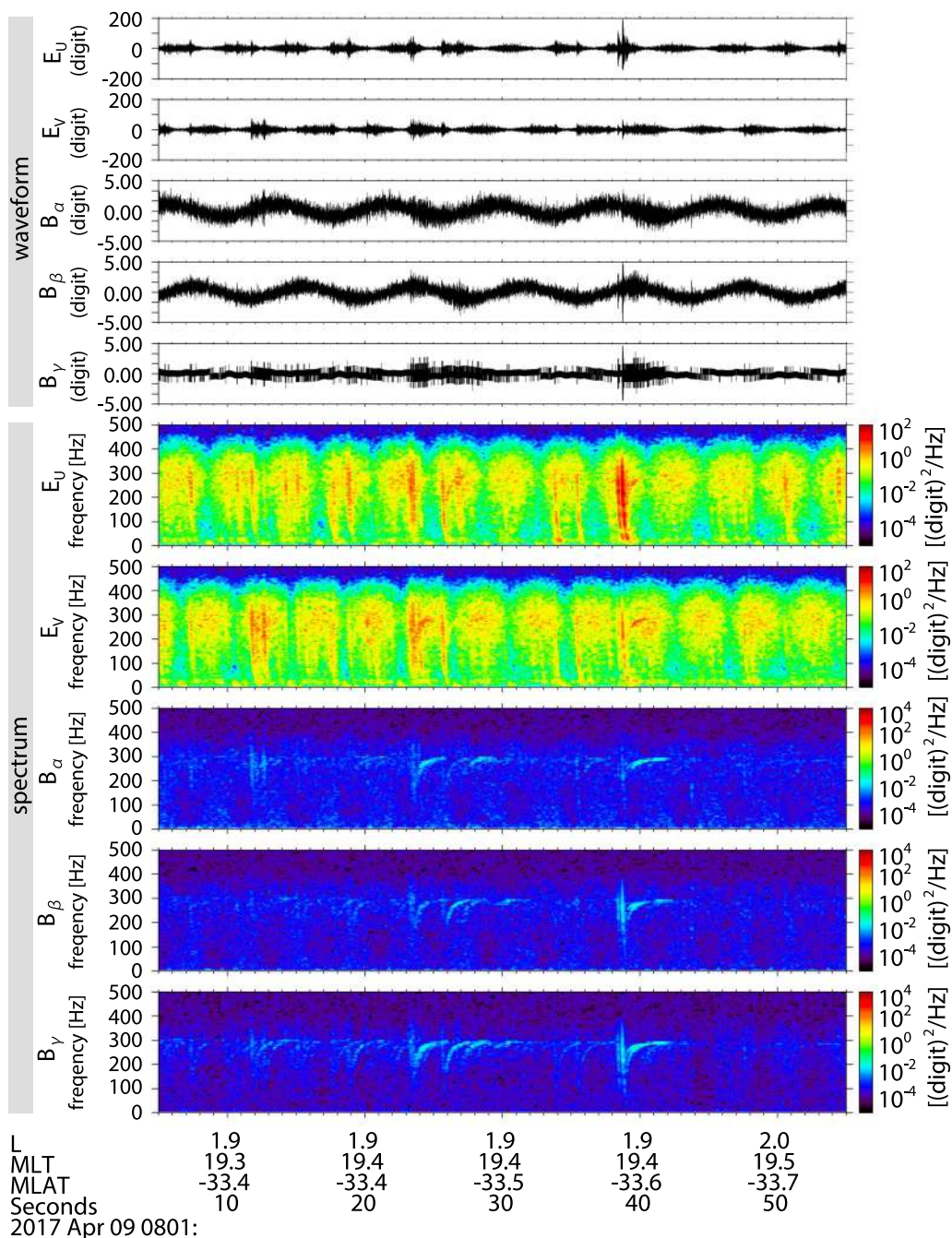
Fig. 20 A sample result of waveform observation by the PWE/WFC in EMIC burst mode from 08:01:05 to 08:01:55 UT on April 9, 2017

complex spectra every 4–32 s. The pseudo-logarithm frequency table achieved data reduction with the spectra observed by the OFA. The initial results show that our onboard processing enables us to clarify detailed properties (e.g., power, propagation direction, and polarization) of the observed plasma waves. The WFC successfully measures raw (chorus burst mode, 65,536 samples/s) and down-sampled (EMIC burst mode, 1024 samples/s) waveforms. We confirmed that the 'chorus burst mode' and 'EMIC burst mode' were suitable for the observation of whistler-mode chorus waves and EMIC mode waves as designed.

Matsuda *et al. Earth, Planets and Space* (2018) 70:75

Page 21 of 22

Author details

[1] Institute for Space-Earth Environmental Laboratory, Nagoya University, Chikusa-ku, Nagoya 464-8601, Japan. [2] Graduate School of Natural Science and Technology, Kanazawa University, Kakuma-machi, Kanazawa 920-1192, Japan. [3] Research Institute for Sustainable Humanosphere, Kyoto University, Gokasho, Uji 611-0011, Japan. [4] Graduate School of Science, Tohoku University, Aoba, Sendai 980-8578, Japan. [5] Department of Information Systems Engineering, Toyama Prefectural University, Kurokawa, Imizu 939-0398, Japan. [6] Institute of Space and Astronautical Science, Yoshinodai, Sagamihara 252-5210, Japan.

Competing interests

The authors declare that they have no competing interests.

Ethics approval and consent to participate

Not applicable.

Publisher's Note

Springer Nature remains neutral with regard to jurisdictional claims in published maps and institutional affiliations.

References

Albert JM (2003) Evaluation of quasi-linear diffusion coefficients for EMIC waves in a multispecies plasma. J Geophys Res 108(A6):1249. https://doi.org/10.1029/2002JA009792

Cornwall JM (1965) Cyclotron instabilities and electromagnetic emission in the ultra low frequency and very low frequency ranges. J Geophys Res 70(1):61–69. https://doi.org/10.1029/JZ070i001p00061

Foster JC, Erickson PJ, Omura Y, Baker DN, Kletzing CA, Claudepierre SG (2017) Van Allen Probes observations of prompt MeV radiation belt electron acceleration in nonlinear interactions with VLF chorus. J Geophys Res Space Phys 122:324–339. https://doi.org/10.1002/2016JA023429

Gendrin R, Ashour-Abdalla M, Omura Y, Quest K (1984) Linear analysis of ion cyclotron interaction in a multicomponent plasma. J Geophys Res 89(A10):9119–9124. https://doi.org/10.1029/JA089iA10p09119

Gomberoff L, Neira R (1983) Convective growth rate of ion-cyclotron waves in a H^+–He^+ and H^+–He^+–O^+ plasma. J Geophys Res 88:2170

Grison B, Darrouzet F, Santolík O, Cornilleau-Wehrlin N, Masson A (2016) Cluster observations of reflected EMIC-triggered emission. Geophys Res Lett. https://doi.org/10.1002/2016GL069096

Hashimoto K, Iwai H, Ueda Y, Kojima H, Matsumoto H (2003) Software wave receiver for the SS-520-2 rocket experiment. IEEE Trans Geosci Remote Sens 41:2638–2647

Hikishima M, Kojima H, Katoh Y, Kasahara Y, Kasahara S, Mitani T, Higashio N, Matsuoka A, Miyoshi Y, Asamura K, Takashima T, Kitahara M, Matsuda S (2018) Data processing in the software-type wave–particle interaction analyzer on board the Arase satellite. Earth Planets Space. https://doi.org/10.1186/s40623-018-0856-y

Horne R, Thorne RM (1998) Potential waves for relativistic electron scattering and stochastic acceleration during magnetic storms. Geophys Res Lett 25:3011–3014

Jordanova VK, Spasojevic M, Thomsen MF (2007) Modeling the electromagnetic ion cyclotron wave-induced formation of detached subauroral proton arcs. J Geophys Res 112:A08209. https://doi.org/10.1029/2006JA012215

Kasaba Y, Ishisaka K, Kasahara Y, Imachi T, Yagitani S, Kojima H, Matsuda S, Shoji M, Kurita S, Hori T, Shinbori A, Teramoto M, Miyoshi Y, Nakagawa T, Takahashi N, Nishimura Y, Matsuoka A, Kumamoto A, Tsuchiya F, Nomura R (2017) Wire Probe Antenna (WPT) and Electric Field Detector (EFD) of Plasma Wave Experiment (PWE) aboard Arase: specifications and initial evaluation results. Earth Planets Space. https://doi.org/10.1186/s40623-017-0760-x

Kasahara Y, Kenmochi H, Kimura I (1994) Propagation characteristics of the ELF emissions observed by the satellite Akebono in the magnetic equatorial region. Radio Sci 29(4):751–767. https://doi.org/10.1029/94RS00445

Kasahara Y, Kasaba Y, Kojima H, Yagitani S, Ishisaka K, Kumamoto A, Tsuchiya F, Ozaki M, Matsuda S, Imachi T, Miyoshi Y, Hikishima M, Katoh Y, Ota M, Shoji M, Matsuoka A, Shinohara I (2018) The Plasma Wave Experiment (PWE) on board the Arase (ERG) Satellite. Earth Planets Space. https://doi.org/10.1186/s40623-018-0842-4

Katoh Y, Omura Y (2007) Relativistic particle acceleration in the process of whistler-mode chorus wave generation. Geophys Res Lett 34:L13102. https://doi.org/10.1029/2007GL029758

Katoh Y, Kojima H, Hikishima M, Takashima T, Asamura K, Miyoshi Y, Kasahara Y, Kasahara S, Mitani T, Higashio N, Matsuoka A, Ozaki M, Yagitani S, Yokota S, Matsuda S, Kitahara M, Shinohara I (2018) Software-type wave–particle interaction analyzer on board the Arase satellite. Earth Planets Space. https://doi.org/10.1186/s40623-017-0771-7

Kumamoto A, Tsuchiya F, Kasahara Y, Kasaba Y, Kojima H, Yagitani S, Ishisaka K, Imachi T, Ozaki M, Matsuda S, Shoji M, Matsuoka A, Katoh Y, Miyoshi Y, Obara T (2018) High Frequency Analyzer (HFA) of plasma wave experiment (PWE) onboard the Arase spacecraft. Earth Planets Space. https://doi.org/10.1186/s40623-018-0854-0

Li W, Thorne RM, Bortnik J, Shprits YY, Nishimura Y, Angelopoulos V, Chaston C, Le Contel O, Bonnell JW (2011) Typical properties of rising and falling tone chorus waves. Geophys Res Lett 38:L14103. https://doi.org/10.1029/2011GL047925

Li W, Thorne RM, Ma Q, Ni B, Bortnik J, Baker DN, Spence Harlan E, Reeves GD, Kanekal SG, Green JC, Kletzing CA, Kurth WS, Hospodarsky GB, Blake JB, Fennell Joseph F, Claudepierre SG (2014) Radiation belt electron acceleration by chorus waves during the 17 March 2013 storm. J Geophys Res Space Phys 119:4681–4693. https://doi.org/10.1002/2014JA019945

Lyons LR, Thorne RM, Kennel CF (1972) Pitch-angle diffusion of radiation belt electrons within the plasmasphere. J Geophys Res 77(19):3455–3474. https://doi.org/10.1029/JA077i019p03455

Martinez-Calderon C, Shiokawa K, Miyoshi Y, Keika K, Ozaki M, Schofield I, Connors M, Kletzing C, Hanzelka M, Santolík O, Kurth WS (2016) ELF/VLF wave propagation at subauroral latitudes: conjugate observation between the ground and Van Allen Probes A. J Geophys Res Space Phys 121:5384–5393. https://doi.org/10.1002/2015JA022264

Matsuda S, Kasahara Y, Goto Y (2014) High-altitude M/Q=2 ion cyclotron whistlers in the inner magnetosphere observed by the Akebono Satellite. Geophys Res Lett 41:3759–3765. https://doi.org/10.1002/2014GL060459

Matsuda S, Kasahara Y, Goto Y (2015) M/Q = 2 ion distribution in the inner magnetosphere estimated from ion cyclotron whistler waves observed by the Akebono satellite. J Geophys Res Space Phys 120:2783–2795. https://doi.org/10.1002/2014JA020972

Matsuda S, Kasahara Y, Kletzing CA (2016) Variation in crossover frequency of EMIC waves in plasmasphere estimated from ion cyclotron whistler waves observed by Van Allen Probe A. Geophys Res Lett 43:28–34. https://doi.org/10.1002/2015GL066893

Matsuoka A, Teramoto M, Nomura R, Nosé M, Fujimoto A, Tanaka Y, Shinohara M, Nagatsuma T, Shiokawa K, Obana Y, Miyoshi Y, Mita M, Takashima T, Shinohara I (2017) The Arase(ERG) magnetic field investigation. Earth Planets Space. https://doi.org/10.1186/s40623-018-0800-1

Matsuda *et al. Earth, Planets and Space* (2018) 70:75

Page 22 of 22

Mauk BH (1982) Helium resonance and dispersion effects on geostationary Alfven/ion cyclotron waves. J Geophys Res 87(A11):9107–9119. https://doi.org/10.1029/JA087iA11p09107

Meredith NP, Thorne RM, Horne RB, Summers D, Fraser BJ, Anderson RR (2003) Statistical analysis of relativistic electron energies for cyclotron resonance with EMIC waves observed on CRRES. J Geophys Res 108(A6):1250. https://doi.org/10.1029/2002JA009700

Meredith NP, Horne RB, Kersten T, Fraser BJ, Grew RS (2014) Global morphology and spectral properties of EMIC waves derived from CRRES observations. J Geophys Res Space Phys 119:5328–5342. https://doi.org/10.1002/2014JA020064

Miyoshi Y, Ono T, Takashima T, Asamura K, Hirahara M, Kasaba Y, Matsuoka A, Kojima H, Shiokawa K, Seki K, Fujimoto M, Nagatsuma T, Cheng CZ, Kazama Y, Kasahara S, Mitani T, Matsumoto H, Higashio N, Kumamoto A, Yagitani S, Kasahara Y, Ishisaka K, Blomberg L, Fujimoto A, Katoh Y, Ebihara Y, Omura Y, Nosé M, Hori T, Miyashita Y, Tanaka Y-M, Segawa T, and ERG Working Group (2012) The Energization and Radiation in Geospace (ERG) Project. In: Summers D, Mann IR, Baker DN, Schulz M (eds) Dynamics of the Earth's radiation belts and inner magnetosphere, pp 103–116. https://doi.org/10.1029/2012GM001304

Miyoshi Y, Oyama S, Saito S, Kurita S, Fujiwara H, Kataoka R, Ebihara Y, Kletzing C, Reeves G, Santolik O, Clilverd M, Rodger CJ, Turunen E, Tsuchiya F (2015) Energetic electron precipitation associated with pulsating aurora: EISCAT and Van Allen Probe observations. J Geophys Res Space Phys 120:2754–2766. https://doi.org/10.1002/2014JA020690

Nakamura S, Omura Y, Shoji M, Nosé M, Summers D, Angelopoulos V (2015) Subpacket structures in EMIC rising tone emissions observed by the THEMIS probes. J Geophys Res Space Phys 120:7318–7330. https://doi.org/10.1002/2014JA020764

Ozaki M, Yagitani S, Sawai K, Shiokawa K, Miyoshi Y, Kataoka R, Ieda A, Ebihara Y, Connors M, Schofield I, Katoh Y, Otsuka Y, Sunagawa N, Jordanova VK (2015) A direct link between chorus emissions and pulsating aurora on timescales from milliseconds to minutes: a case study at subauroral latitudes. J Geophys Res Space Phys 120:9617–9631. https://doi.org/10.1002/2015JA021381

Ozaki M, Yagitani S, Kasahara Y, Kojima H, Kasaba Y, Kumamoto A, Tsuchiya F, Matsuda S, Matsuoka A, Sasaki T, Yumoto T (2018) Magnetic Search Coil (MSC) of Plasma Wave Experiment (PWE) aboard the Arase (ERG) satellite. Earth Planets Space. https://doi.org/10.1186/s40623-018-0837-1

Perraut S, Roux A, Robert P, Gendrin R, Sauvaud J-A, Bosqued J-M, Kremser G, Korth A (1982) A systematic study of ULF waves Above FH+ from GEOS 1 and 2 measurements and their relationships with proton ring distributions. J Geophys Res 87(A8):6219–6236. https://doi.org/10.1029/JA087iA08p06219

Pickett JS, Grison B, Omura Y, Engebretson MJ, Dandouras I, Masson A, Adrian ML, Santolík O, Décréau PME, Cornilleau-Wehrlin N, Constantinescu D (2010) Cluster observations of EMIC triggered emissions in association with Pc1 waves near Earth's plasmapause. Geophys Res Lett 37:L09104. https://doi.org/10.1029/2010GL042648

Reeves GD, Spence HE, Henderson MG, Morley SK, Friedel RHW, Funsten HO, Baker DN, Kanekal SG, Blake JB, Fennell JF, Claudepierre SG, Thorne RM, Turner DL, Kletzing CA, Kurth WS, Larsen BA, Niehof JT (2013) Electron acceleration in the heart of the Van Allen radiation belts. Science 341:991–994. https://doi.org/10.1126/science.1237743

Sakaguchi K, Kasahara Y, Shoji M, Omura Y, Miyoshi Y, Nagatsuma T, Kumamoto A, Matsuoka A (2013) Akebono observations of EMIC waves in the slot region of the radiation belts. Geophys Res Lett 40:5587–5591. https://doi.org/10.1002/2013GL058258

Santolík O, Parrot M, Lefeuvre F (2003a) Singular value decomposition methods for wave propagation analysis. Radio Sci 38:1010. https://doi.org/10.1029/2000RS002523

Santolík O, Gurnett DA, Pickett JS, Parrot M, Cornilleau-Wehrlin N (2003b) Spatio-temporal structure of storm-time chorus. J Geophys Res 108:1278. https://doi.org/10.1029/2002JA009791

Santolík O, Gurnett DA, Pickett JS, Parrot M, Cornilleau-Wehrlin N (2004) A microscopic and nanoscopic view of storm-time chorus on 31 March 2001. Geophys Res Lett 31:L02801. https://doi.org/10.1029/2003GL018757

Shiokawa K, Kato Y, Hamaguchi Y, Yamamoto Y, Adachi T, Ozaki M, Oyama S-I, Nose M, Nagatsuma T, Tanaka Y, Otsuka Y, Miyoshi Y, Kataoka R, Takagi Y, Takeshita Y, Shinbori A, Kurita S, Hori T, Nishitani N, Shinohara I, Tsuchiya F, Obara Y, Suzuki S, Takahashi N, Seki K, Kadokura A, Hosokawa K, Ogawa Y, Connors M, Ruohoniemi JM, Engebretoson M, Turunen E, Ulich T, Manninen J, Raita T, Kero A, Oksanen A, Back M, Kauristie K, Mattanen J, Baishev D, Kurkin V, Oinats A, Pashinin A, Vasilyev R, Rakhmatulin R, Bristow W, Karjala M (2017) Ground-based instruments of the PWING project to investigate dynamics of the inner magnetosphere at subauroral latitudes as a part of the ERG-ground coordinated observation network. Earth Planets Space. https://doi.org/10.1186/s40623-017-0745-9

Summers D, Tang R, Omura Y (2012) Linear and nonlinear growth of magnetospheric whistler mode waves. In: Summers D, Mann IR, Baker DN, Schulz M (eds) Dynamics of the Earth's radiation belts and inner magnetosphere. American Geophysical Union, Washington. https://doi.org/10.1029/2012GM001298

Thorne RM, Kennel CF (1971) Relativistic electron precipitation during magnetic storm main phase. J Geophys Res 76(19):4446–4453. https://doi.org/10.1029/JA076i019p04446

Tsurutani BT, Smith EJ (1974) Postmidnight chorus: a substorm phenomenon. J Geophys Res 79(1):118–127. https://doi.org/10.1029/JA079i001p00118

Walker SN, Balikhin MA, Shklyar DR, Yearby KH, Canu P, Carr CM, Dandouras I (2015) Experimental determination of the dispersion relation of magnetosonic waves. J Geophys Res Space Phys 120:9632–9650. https://doi.org/10.1002/2015JA021746